

## RESEARCH ARTICLE

# Hyperphosphorylated tau in Alzheimer's disease disseminates along pathways predicted by the Structural Model for Cortico-cortical Connections

Alicia Uceda-Heras<sup>1,2</sup>  | Gonzalo Aparicio-Rodríguez<sup>1,3</sup>  | Miguel Ángel García-Cabezas<sup>1,2,3,4</sup> 

<sup>1</sup>Department of Anatomy, Histology and Neuroscience, School of Medicine, Autónoma University of Madrid, Madrid, Spain

<sup>2</sup>PhD Program in Neuroscience UAM-Cajal, Autónoma University of Madrid, Madrid, Spain

<sup>3</sup>Master's Program in Neuroscience, Autónoma University of Madrid, Madrid, Spain

<sup>4</sup>Neural Systems Laboratory, Department of Health Sciences, Boston University, Boston, Massachusetts, USA

## Correspondence

Miguel Ángel García-Cabezas, Departamento de Anatomía, Histología y Neurociencia, Calle Arzobispo Morcillo 4, 28029 Madrid, Spain.  
Email: [garcia.cabezas@uam.es](mailto:garcia.cabezas@uam.es)

## Funding information

Ministerio de Ciencia, Innovación y Universidades, Grant/Award Number: BEAGAL18/00098; Comunidad de Madrid, Grant/Award Number: SI2/PBG/2020-00014

## Abstract

In Alzheimer's disease (AD), hyperphosphorylated tau spreads along the cerebral cortex in a stereotypical pattern that parallels cognitive deterioration. Tau seems to spread transsynaptically along cortico-cortical pathways that, according to synaptic tract-tracing studies in nonhuman primates, have specific laminar patterns related to the cortical type of the connected areas. This relation is described in the Structural Model. In the present article, we study the laminar distribution of hyperphosphorylated tau, labeled with the antibody AT8, along temporal cortical types in postmortem human brains with different AD stages to test the predictions of the Structural Model. Brains from donors without dementia had scant AT8-immunoreactive (AT8-ir) neurons in allo-, meso-, and isocortical types. In early AD stages, the mesocortical dysgranular type, including part of the transentorhinal cortex, had the highest AT8 immunostaining and AT8-ir neurons density. In advanced AD stages, AT8 immunostaining increased along the isocortical types until reaching the auditory koniocortex. Regarding laminar patterns, in early AD stages there were more AT8-ir neurons in supragranular layers in each de novo involved neocortical type; in advanced AD stages, AT8-ir neurons were equally distributed in supra- and infragranular layers. These AT8-ir laminar patterns are compatible with the predictions of the Structural Model. In summary, we show that hyperphosphorylated tau initially accumulates in allo-, meso-, and isocortical types, offer a proof of concept for the validity of the Structural Model to predict synaptic pathway organization in the human cerebral cortex, and highlight the relevance of nonhuman primate tract-tracing studies to understand human neuropathology.

## KEYWORDS

allocortex, cerebral cortex, cortical type, eulamine, isocortex, mesocortex, neocortex

This is an open access article under the terms of the [Creative Commons Attribution](https://creativecommons.org/licenses/by/4.0/) License, which permits use, distribution and reproduction in any medium, provided the original work is properly cited.

© 2024 The Authors. The *Journal of Comparative Neurology* published by Wiley Periodicals LLC.

## 1 | INTRODUCTION

Alzheimer's disease (AD) is a neurodegenerative disorder in which synapses and neurons are progressively lost causing gradual cognitive deterioration. In parallel to neuron loss, two misfolded proteins aggregate and accumulate in the nervous tissue: A $\beta$  amyloid accumulates extracellularly in neuritic plaques and small blood vessel walls; and the microtubule associated protein tau forms neurofibrillary tangles and neuropil threads in the cytoplasm of neurons (Calderon-Garcidueñas & Duyckaerts, 2017). As AD progresses, hyperphosphorylated tau inclusions spread along the cerebral cortex in a stereotypical pattern that is correlated with the level of cognitive deterioration (the more tau inclusions spread, the more cognition deteriorates). Thus, the quantification of hyperphosphorylated tau spread in postmortem human brains is used for AD staging (Braak et al., 2006; Braak & Braak, 1991). The beginning of tau hyperphosphorylation and aggregation in the cerebral cortex has been traced to transentorhinal areas of the temporal lobe (Braak & Braak, 1997), which are mesocortical areas that lie adjacent to the entorhinal allocortex, have simple laminar architecture, and lack or have rudimentary inner granular layer IV. From mesocortical areas, hyperphosphorylated tau inclusions spread to isocortical areas of more complex laminar architecture with well-developed layer IV. The complexity of laminar architecture and the development of layer IV increase progressively along isocortical areas and culminate in koniocortices, which are the cortical areas of most complex laminar architecture. Hyperphosphorylated tau spreads to koniocortical areas in the most advanced stages of AD (Arnold et al., 1991; Braak et al., 2006). In summary, as AD progresses, hyperphosphorylated tau inclusions spread along the cortical gradient of increasing laminar complexity from the meso- to the koniocortical areas.

It is supposed that hyperphosphorylated tau spreads transsynaptically in AD along cortico-cortical pathways following a prion-like process (Braak & Del Tredici, 2011). Even more, it has been suggested that hyperphosphorylated tau spreads along top-down projections from areas at higher levels in the cortical hierarchy to areas in the lower levels (Braak & Del Tredici, 2018). A key point to understand the progression of AD is that cortico-cortical pathways are not random, but follow principles that have been identified in synaptic tract-tracing studies in nonhuman primates and summarized in a relational model called the Structural Model for Cortico-cortical Connections (Aparicio-Rodríguez & García-Cabezas, 2023; Barbas & Rempel-Clower, 1997; García-Cabezas et al., 2019). This model relates the laminar patterns of cortico-cortical connections to the laminar architecture of the connected areas. Thus, pathways from areas of simpler to areas of more complex laminar architecture are originated in infragranular (V–VI) layers and terminate in superficial (I–III) layers. On the reverse direction, pathways from areas of more complex architecture to areas of simpler laminar architecture are originated in supragranular (II–III) layers and terminate in middle-deep (IV–VI) layers. The pathways that connect areas of comparable laminar complexity are originated in supra- (II–III) and infragranular (V–VI) layers and terminate across all layers (I–VI). Therefore, by knowing the degree of laminar complexity of two

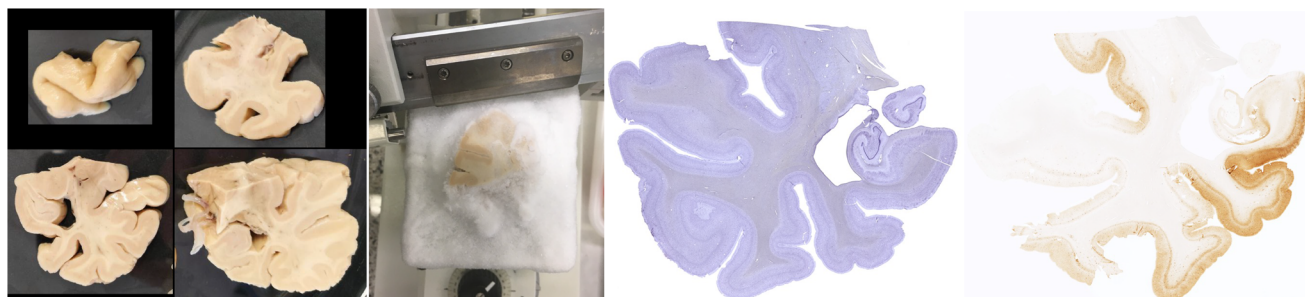
cortical areas it is possible to predict the laminar pattern of the synaptic connections between them. These laminar patterns are not trivial because they are associated to the flow of information along cortical hierarchies (Felleman & Van Essen, 1991); thus, pathways from areas of simpler to areas of more complex architecture are feedback, or top-down, and pathways from areas of more complex to areas of simpler architecture are feedforward, or bottom-up (Chanes & Barrett, 2016; Hilgetag & Goulas, 2020).

The principles of the Structural Model can be applied to the human cerebral cortex using the conceptual tool of cortical type. Operationally, several cortical types can be defined along the human cortical gradient of laminar complexity: from the simplest allocortex to the most complex koniocortex (García-Cabezas et al., 2020; Sancha-Velasco et al., 2023). These types and the principles of the Structural Model allow to hypothesize the laminar patterns of cortico-cortical connections between human cortical areas. Such hypothesis could be tested by checking the laminar spreading of hyperphosphorylated tau inclusions in AD.

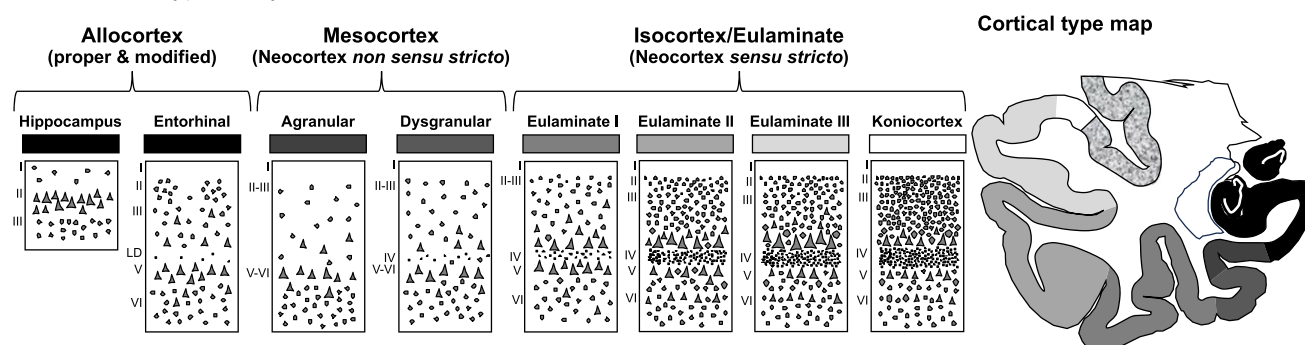
In the present article, we aim to test the predictions of the Structural Model for Cortico-cortical Connections in the human cerebral cortex. For this purpose, we assume the hypothesis of transsynaptic dissemination of hyperphosphorylated tau and study its laminar distribution along the human temporal lobe in postmortem brains with different AD stages. First, we review the literature on the Structural Model and summarize its major principles, including the phylogenetic origin of primate cortical types. Second, we use immunohistochemistry with the monoclonal antibody AT8, which labels hyperphosphorylated tau, to quantify tau inclusion spread in the temporal lobe of postmortem human brains from donors without dementia and with confirmed diagnosis of AD. Finally, we quantify hyperphosphorylated tau spreading in supra and infragranular layers of the temporal neocortex to identify laminar patterns of spreading and compare them to the predictions of laminar patterns of synaptic connections according to the Structural Model. In several brains from donors without dementia, there were scant AT8-immunoreactive (AT8-ir) neurons in the allocortex (hippocampus and entorhinal cortex), in adjacent mesocortical, and in isocortical areas. In early AD stages, the dysgranular type of the temporal mesocortex, which includes part of the transentorhinal cortex, had the highest density of AT8 immunostaining and AT8-ir neurons. In more advanced AD stages, hyperphosphorylated tau pathology spread along the isocortical types until reaching the auditory koniocortex. Also, AT8-ir neurons were found preferentially in supragranular layers of each de novo involved neocortical type in the earliest Braak stages; in more advanced stages, AT8-ir neurons were equally distributed in supra- and infragranular layers. These laminar patterns of hyperphosphorylated tau spreading along neocortical areas (early in supragranular; late in supra- and infragranular layers) are compatible with the laminar patterns of cortico-cortical synaptic connections predicted by the Structural Model. In summary, the present study shows that hyperphosphorylated tau initially accumulates in allo- and isocortical areas in addition to the mesocortical transentorhinal cortex, offers a proof of concept for the validity of the Structural Model for Cortico-cortical Connections to draw predictions for synaptic pathway organization in

(a) Review of the literature on the **Structural Model for Cortico-cortical Connections**Review of the literature on the **Hypothesis on the Dual Origin of the Neocortex**

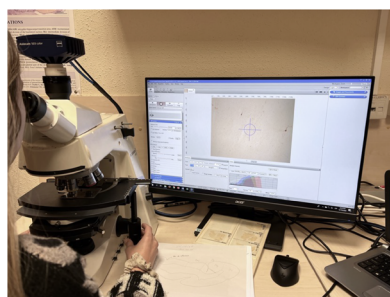
## (b) Brain tissue obtention, blocking, cutting, and staining



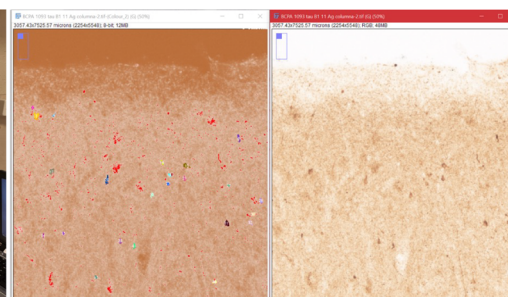
## (c) Cortical type analysis



## (d) Micrography



## (e) Tau quantification



## (f) Data curation and statistics

	A	B	C	D	E	F	G	H
	Brain ID	Donor Age	Donor Sex	Brain stage	Cortical type	Layers I-VI OD	OD Supragranular	OD Infragranular
1	28-M-67	67	Male	I	Agranular	30107957.43	23370745.32	30903661.89
2	28-M-67	67	Male	I	Agranular	65237409.16	56410436.84	65717382.72
3	28-M-67	67	Male	I	Agranular	25998084.54	13098639.73	36213816.77
4	28-M-67	67	Male	I	Agranular	56801773.28	34292962.19	66628098.26
5	28-M-67	67	Male	I	Dysgranular	45236034.89	52907389.4	31687940.86
6	28-M-67	67	Male	I	Dysgranular	154402139.1	213008050	75807226.17
7	28-M-67	67	Male	I	Dysgranular	38470951.9	40405092.43	27987491.54
8	28-M-67	67	Male	I	Dysgranular	65159450.9	69669289.94	52783966.45
9	28-M-67	67	Male	I	Eulaminar I	27848613.91	29105366.39	20321563.77
10	28-M-67	67	Male	I	Eulaminar I	43294304.56	45080095.77	28852017.52
11	28-M-67	67	Male	I	Eulaminar I	32295405.46	35184957.35	22421165.26
12	28-M-67	67	Male	I	Eulaminar I	42934155.92	51109111.82	26432942.74
13	28-M-67	67	Male	I	Eulaminar I	24545507.2	38096717.9	308101027.2
14	BCPA BAD	85	Female	II	Agranular	355629364.1	482134125.7	325015128.2
15	BCPA BAD	85	Female	II	Agranular	48332804.95	63620020.55	59491454.45
16	BCPA BAD	85	Female	II	Dysgranular	288647069	462336079.4	136091025.5
17	BCPA BAD	85	Female	II	Dysgranular	7944623.013	11192086.9	19606996.56
18	BCPA BAD	85	Female	II	Eulaminar I	89086548.84	120586294.6	70815286.58
19	BCPA BAD	85	Female	II	Eulaminar I	5042079.528	8978523.3	13569801.08
20	BCPA BAD	85	Female	II	Eulaminar I	3301844.781	647897.34	6869978.5
21	BCPA BAD	85	Female	II	Eulaminar I	14442254.55	11002985.4	13618737.52
22	BCPA BAD	85	Female	II	Eulaminar I	33626078.59	38801542.65	27435073.99

**FIGURE 1** Experimental design. (a) Review of the literature on the Structural Model for Cortico-cortical Connections and the Hypothesis of the Dual Origin of the Neocortex. (b) Brain tissue obtention, blocking, cutting, and staining with Nissl technique and immunohistochemistry with the monoclonal AT8 antibody. (c) Cortical type analysis; several cortical types are defined along the gradient of laminar complexity: two allocortical (proper and modified), two mesocortical (neocortex *non sensu stricto*), and four isocortical/eulaminar (neocortex *sensu stricto*) types; cortical types can be represented with grayscale on maps (far right cartoon). (d) Micrography of stained tissue. (e) AT8 immunostaining quantification on micrographs using Image j. (f) Data curation and statistical analysis.

the human cerebral cortex, and highlights the relevance on nonhuman primate tract-tracing studies to understand human neuropathology.

## 2 | MATERIALS AND METHODS

### 2.1 | Experimental design

The experimental design is summarized in Figure 1. First, we reviewed the literature on the Structural Model for Cortico-cortical Connections,

summarize its major principles, and trace the roots of the primate gradient of laminar complexity in forebrain evolution within the Hypothesis on the Dual Origin of the Neocortex (Figure 1a). Second, we collected postmortem human brain tissue containing the temporal lobe from donors with and without dementia; the brains with dementia had been postmortem diagnosed of AD. Brain samples were blocked, cut, and stained for Nissl technique and immunohistochemistry with the monoclonal antibody AT8 that labels hyperphosphorylated tau (Figure 1b). Third, we performed cortical type analysis in Nissl-stained sections (Figure 1c). Fourth, we took micrographs of representative

columns of each cortical type in AT8-immunostained sections from each brain (Figure 1d) and used Image J to quantify overall hyperphosphorylated AT8 immunostaining and AT8-ir neurons (Figure 1e). AT8 immunostaining was also used for Braak staging (Braak et al., 2006). Finally, the data were exported to Excel and curated for statistical analysis and graph elaboration (Figure 1f).

## 2.2 | Literature review

We reviewed the articles in which the Structural Model for Cortico-cortical Connections was proposed and developed. We reviewed the articles of Helen Barbas, the first proponent of the Structural Model, and of her coworkers who have further developed this model, specifically, Claus Hilgetag, Basilis Zikopoulos, Maria Medalla, and Miguel Ángel García-Cabezas. We summarize the principles of the Structural Model and trace the phylogenetic origin of the primate gradient of laminar complexity within the Hypothesis on the Dual Origin of the Neocortex (García-Cabezas et al., 2023a).

## 2.3 | Postmortem human brains: Obtention and tissue processing

We used brain tissue from eight human donors. Left temporal lobe brain tissue from donors without clinical diagnose of dementia ( $n = 5$ ; female = 2) were retrieved from Dr. Cavada's anonymized brain archives at the Department of Anatomy, Histology, and Neuroscience of the School of Medicine of the Autónoma University of Madrid (Madrid, Spain,  $n = 3$ ; female = 1; brains 11/F/30, 21/M/58, 28/M/67), the *Plataforma Biobanco—Instituto Murciano de Investigación Biosanitaria Pascual Parrilla* (<https://biobanco.imib.es/grupoinvestigacion/index.jsf>, Murcia, Spain,  $n = 1$ ; male; brain BCM 261), and the *Banco de Tejidos de la Fundación CIEN* (<https://bt.fundacioncien.es/>, Madrid, Spain,  $n = 1$ ; female = 1; brain BCPA 840). Left temporal lobe brain tissue from donors with clinical diagnose of dementia and postmortem diagnose of AD were obtained from the *Banco de Tejidos de la Fundación CIEN* (Madrid, Spain,  $n = 3$ ; female = 1; brains BCPA 392, BCPA 991, BCPA 1093). The use of human brain tissue for the present study was approved by the Ethics Committee for Research of Autonomous University of Madrid (Authorization CEI-104-2011). Table 1 summarizes the data of all the studied brains.

Tissue from the anonymized brains in Dr. Cavada's archives has been used in previous publications (García-Cabezas et al., 2007; Sancha-Velasco et al., 2023). These brains were extracted in clinical autopsies and fixed with formaldehyde (4% in PB, 0.1 M) by vascular perfusion, hemisected through the sagittal plane, and cut stereotaxically in 1-cm coronal slabs (for details, see García-Cabezas et al., 2023b); slabs were postfixed in the same fixative solution for 24 h, cryoprotected by immersion in gradually increasing concentrations of sucrose (in PB, 0.1 M) until they sank, and preserved in ethylene-glycol solution at  $-20^{\circ}\text{C}$  until smaller blocks containing the temporal lobe were obtained for microtome sectioning. The brains from *Plataforma*

*Biobanco—Instituto Murciano de Investigación Biosanitaria Pascual Parrilla* and *Banco de Tejidos de la Fundación CIEN* were fixed by immersion in 10% formalin and preserved in the same solution. Upon arrival to our laboratory, temporal lobes were photographed, blocked coronally, and cryoprotected by immersion in gradually increasing concentrations of sucrose (in PB, 0.1 M) until they sank.

All the left temporal lobe coronal blocks were cut on a freezing microtome into coronal sections of 50  $\mu\text{m}$  thickness and collected in 10 consecutive series. One series of sections from each block was mounted in gelatin-coated slides (Gelatine 80–100 Blooms, Pan-reac; Barcelona, Spain) and stained for Nissl using cresyl violet. The sections that were not selected immediately for staining were stored at  $-20^{\circ}\text{C}$  in an ethylene-glycol solution for several weeks or months.

## 2.4 | Antibody characterization and immunohistochemistry

Selected sections representative of four anterior–posterior levels of each left temporal lobe (temporal pole, amygdala, anterior hippocampus, and posterior hippocampus) were processed for immunohistochemistry with the monoclonal antibody AT8 that labels hyperphosphorylated tau [Anti-Phospho-Tau (Ser202, Thr205) mouse monoclonal antibody AT8, Catalogue # MN1020; RRID AB\_223647; ThermoFisher Scientific, Waltham, MA, USA]. AT8 antibody labels phosphorylated tau at both serine 202 and threonine 205, does not cross-react with normal tau epitopes, and renders reliable immunostaining in postmortem human brain tissue regardless of fixation and/or tissue preservation time in formaldehyde (Alafuzoff et al., 2008; Braak et al., 2006; Goedert et al., 1995).

We briefly describe the immunohistochemistry method for AT8. All the sections from the eight brains used in the present study were processed at the same time to minimize differences in immunostaining due to procedural variations. Free-floating sections were rinsed in TBS (0.1 M, pH 7.6) and pretreated in a solution of 3%  $\text{H}_2\text{O}_2$  in TBS for 20 min at room temperature to inhibit endogenous peroxidase. Then, sections were rinsed in TBS and placed in sodium citrate buffer (10 mM, pH 6.00), heated for 30 min in a water bath at  $70^{\circ}\text{C}$  for antigen retrieval, and allowed to cool down for 30 min. After antigen retrieval, sections were rinsed in TBS and preblocked [20% normal goat serum (NGS), 5% bovine serum albumin (BSA), and 0.2% Triton-X in TBS] at  $4^{\circ}\text{C}$  for 2 h. Sections were then incubated during 48 h at  $4^{\circ}\text{C}$  in the AT8 primary antibody against hyperphosphorylated tau (diluted 1:500 in TBS with 20% NGS, 5% BSA, and 0.1% Triton-X), rinsed in TBS, and incubated at room temperature for 3 h in the secondary biotinylated goat anti-mouse [Biotin-SP (long spacer) AffiniPure™ Goat Anti-Mouse IgG (H+L); Code: 115-065-003; RRID: AB\_2338557; Jackson ImmunoResearch Europe LTD, Cambridge, UK] diluted 1:1000 in 20% NGS, 5% BSA, and 0.2% Triton-X in TBS. Then, sections were rinsed in TBS followed by 1 h at room temperature in the dark in an avidin–biotin horseradish peroxidase complex (AB-HRP; Vectastain PK-6100 ABC Elite kit, Vector Laboratories, Newark, CA,



**TABLE 1** Brain donor data.

Case	Sex	Age	Dementia	Braak
11/F/30	F	30	No	Pre-Braak
BCM 261	M	46	No	Pre-Braak
21/M/58	M	58	No	Pre-Braak
28/M/67	M	67	No	I
BCPA 840	F	85	No	II
BCPA 1093	M	83	Yes	IV
BCPA 392	M	87	Yes	V
BCPA 991	F	71	Yes	VI

USA; 1 drop of solution A and 1 of solution B in 2.5 mL of TBS). Finally, sections were rinsed in TBS followed by TB (0.1 M, 4°C, pH 7.6) and processed for the peroxidase-catalyzed polymerization of diaminobenzidine (DAB); we diluted DAB tablets (10 mg; 3,3'-diaminobenzidine tetrahydrochloride tablet, D5905-100TAB, Sigma-Aldrich, St. Louis, MO, USA) in TB to obtain a DAB solution of 50 mg DAB/100 mL TB. Sections were incubated in the DAB solution for 15 min at 4°C in the dark followed by incubation in the same solution with 0.03 % H<sub>2</sub>O<sub>2</sub> for 3–5 min under microscope control. After DAB development, sections were washed with PB (0.1 M, pH 7.35), mounted on gelatin-coated slides (Gelatine 80–100 Blooms, Panreac), and coverslipped with mounting media (DePex, Cat # 18243.02; SERVA Electrophoresis GmbH, Heidelberg, Germany).

We also run negative control experiments to test labeling specificity. In these control experiments we did not add the primary antibody AT8 to the incubation solution (TBS with 20% NGS, 5% BSA, and 0.1% Triton-X), but kept all the other steps unchanged.

## 2.5 | Cortical type analysis in the human temporal lobe

In our previous publications, we have explained how to perform cortical type analysis in human brain Nissl-stained sections (García-Cabezas et al., 2020; Sancha-Velasco et al., 2023). Briefly, cortical neurons and glial cells are arranged in layers that run parallel to the brain surface; these layers vary in their number and definition across gradients of progressive laminar complexification from the simplest allocortex to the most complex koniocortex. Several cortical types can be operationally defined along the gradient of laminar complexification. We have defined two mesocortical (neocortex *non sensu stricto*), and four isocortical or eulaminar (neocortex *sensu stricto*) types (Figure 1c; see also García-Cabezas et al., 2020). In the present article, we also consider two allocortical types in the hippocampal formation. First, we categorize the fascia dentata, the cornu ammonis, and the subiculum, which have been traditionally described as archicortex, as “proper allocortex”; these areas have three layers (see figure 12.5 in Nieuwenhuys et al., 2008). Second, we categorize the presubiculum, parasubiculum, and entorhinal cortex, which have been traditionally described

as periarchicortex, as “modified allocortex”; these areas have five or six layers (see figure 12.5 in Nieuwenhuys et al., 2008). Contemporary genoarchitectonic studies have showed that all these areas are specified within the Medial Pallium and have suggested that presubiculum, parasubiculum, and entorhinal cortex are “modified allocortex” (Puelles et al., 2019).

We mapped cortical types in Nissl-stained sections adjacent to AT8-immunostained sections to guide hyperphosphorylated tau quantification in each cortical type. For this purpose, we took low magnification photographs of each Nissl-stained section with and Axiocam 503 color (Zeiss; Oberkochen, Germany) attached to an optical microscope (Axioskop 2 MOT, Zeiss) and a computer with the software Zen (Zeiss); then, we printed the photographs and manually draw on their hard copies the boundaries between types as each section was examined under the optical microscope. These boundaries were transferred to hard copies of low magnification photographs of the adjacent AT8-immunostained sections.

## 2.6 | Postmortem AD staging

We examined the temporal lobe AT8-immunostained sections to perform AD staging according to the criteria of Braak et al. (2006). Brains with AT8 immunostaining that did not meet the criteria for Braak I stage were classified as pre-Braak. Some brains provided by the *Banco de Tejidos de la Fundación CIEN* (BCPA 392, BCPA 840, BCPA 991, BCPA 1093) had been diagnosed with AD by expert neuropathologists.

## 2.7 | AT8 immunostaining quantification

In brains staged from Braak I to Braak VI, we used the Zeiss Axiocam 503 color attached to the Zeiss Axioskop 2 MOT and a computer with the Zeiss Zen software to photograph straight gyral columns of cortical tissue in the entorhinal cortex and all the neocortical types identified in each AT8-immunostained section. For each column, five overlapping micrographs covering the entire cortical thickness were taken at 10x; the “Acquisition-Panorama” and “Processing-Stitching” functions were used to obtain a tiff file for each column. The width of each column was 1.400 μm. All the micrographs were taken under the same microscope

illumination (position 2) and exposure time (50 ms). Tiff files were open in Image J and calibrated with the calibration bar inserted by Zen in each column. Then, we applied to each of them a customized macro function that predetermined the same conditions (brightness, contrast, color deconvolution, vector H DAB, brown channel, Moments dark threshold) for all the tiff files. Next, we used the “Analyze-Measure” function to obtain the integrated density, which we considered optical density (OD), for the entire column (layers I–VI), supra- (I–III), and infragranular (V–VI) layers; for the entorhinal cortex, OD was measured for the entire column only. OD was measured in pixels/ $\mu\text{m}^2$ . The borders of supra- and infragranular layers were delineated in the adjacent Nissl-stained section and transferred to the tiff file using the “Freehand selections” tool.

Also, we quantified AT8-ir neurons. In brains staged as pre-Braak, we quantified manually all the AT8-ir neurons. We also mapped the distribution of these neurons using a computerized analysis system attached to a Zeiss Axioskop microscope (Oberkochen, Germany). The system is composed of a video camera (CX9000 camera; MicroBrightField Bioscience, Williston, VT, USA), a motorized microscope stage (MBF Bioscience, USA; Heidenhain Corporation, USA), and a personal computer, and is driven by the Neurolucida<sup>®</sup> software (MicroBrightField). The drawings were made on a computer screen using the 20 $\times$  objective to identify the AT8-ir neurons. Other elements, like the outer borders of the cerebral cortex and the boundary between the gray and white matter, were also traced. Nissl-stained sections adjacent to the AT8-immunostained sections were used to trace the borders of the cortical types, the upper limit of layer IV in the neocortex, and the lamina dissecans in the entorhinal cortex. The surface contour served as reference mark to transfer the delineated boundaries of types and layers to the AT8-ir neuron maps.

In brains staged from Braak I to Braak VI, we quantified AT8-ir neurons in the micrographs of cortical columns with the same customized macro used for OD quantification. The same parameters were used except for the threshold, which was adapted depending on the Braak stage. Thus, we traced supra- and infragranular layers in the tiff file for each cortical column and used the “Analyze-Particles” function to obtain the number of AT8-ir neurons. Each analyzed cellular profile appeared highlighted on the tiff files with an overlapped mask. Then we checked these profiles one by one; those profiles that did not show cytological features of neuron bodies were deleted; also, some profiles that were not identified by the macro were manually added. We quantified AT8-ir neurons in supra- and infragranular layers (II–III & V–VI), in supragranular (II–III) layers, and in infragranular (V–VI) layers. For the entorhinal cortex, AT8-ir neurons were quantified for the entire column. In neocortical areas, we also computed the fraction of AT8-ir supragranular neurons dividing the count of supragranular AT8-ir neurons by the count of supra- and infragranular AT8-ir neurons.

## 2.8 | Statistical analysis

The data obtained with Image J were exported to Excel for statistical analysis. Data corresponding to each straight gyrus column of cortical

tissue were entered into the following columns: brain ID, donor age, donor sex, Braak stage, cortical type, layers I–VI OD, supragranular (layers I–III) OD, infragranular (layers V–VI) OD, supra- and infragranular (layers II–III and V–VI) AT8-ir neurons, supragranular (layers II–III) AT8-ir neurons, infragranular (layers V–VI) AT8-ir neurons, and fraction of AT8-ir supragranular neurons. Data from Excel were entered into GraphPad Prism software (Version 10.1.2, GraphPad Software) for statistical analysis.

We made two comparisons with the data obtained in each of the three OD quantifications [layers I–VI; supragranular (I–III) layers; infragranular (V–VI) layers] and the four AT8-ir neuron quantifications [supra- and infragranular (I–III and V–VI) layers; supragranular (II–III) layers; infragranular (V–VI) layers; fraction of AT8-ir supragranular neurons]. First, we compared each quantification data between cortical types in each Braak stage. Second, we compared each quantification data between Braak stages in each cortical type. Thus, a total of 14 comparisons were made. We applied the Kolmogorov–Smirnov test to check if each set of data for each of the 14 comparisons followed a normal distribution. Then, we performed a single-factor analysis (one-way ANOVA) with a multiple comparisons test corrected for those nonparametric distributions by controlling the False Discovery Rate with the two-stage step-up method test of Benjamini, Krieger, and Yekutieli. The degrees of significance were set at  $p < .05$  (\*),  $p < .01$  (\*\*), and  $p < .001$  (\*\*\*).

## 2.9 | Figure and graph elaboration

Low power panoramic photographs from Nissl and AT8-immunostained sections were taken with the microscope set up used for mapping AT8-ir neurons in the pre-Braak brains (CX9000 camera and Neurolucida<sup>®</sup> software; MicroBrightField). High power micrographs were taken with the Zeiss AxioCam 503 camera attached to the Zeiss Axioskop 2 MOT microscope using Zeiss Zen software. Graphs were elaborated using GraphPad Prism software and Excel. The data in the graphs corresponding to each Braak stage and cortical type were color coded [Braak I, blue; Braak II, red; Braak IV, green; Braak V, purple; Braak VI, orange; laminar complexity grayscale: from black (simplest cortical type) to lightest gray (most complex type)] and represented in nested scatter plots with bars and plus points. Figures were assembled using PowerPoint software. Several schemes were drawn using the Shape tools in the same software.

## 3 | RESULTS

### 3.1 | Principles of cortico-cortical connections according to the Structural Model

We retrieved eleven experimental tract-tracing studies in macaques and six theoretical reviews by Helen Barbas and her coworkers (Claus Hilgetag, Basilis Zikopoulos, Maria Medalla, and Miguel Ángel García-Cabezas). The retrieved articles are summarized in Table 2. The relation

**TABLE 2** Experimental and theoretical articles on the Structural Model.

Reference	Cortical areas injected	Cortical region studied
Barbas (1986)	Meso- and isocortical prefrontal areas	Entire cerebral cortex
Barbas and Rempel-Clover (1997)	Meso- and isocortical prefrontal areas	Prefrontal cortex
Rempel-Clover and Barbas (2000)	Meso- and isocortical prefrontal and temporal areas	Prefrontal and temporal cortex
Medalla and Barbas (2006)	Isocortical prefrontal areas	Isocortical posterior parietal areas
Hilgetag et al. (2016)	Visual temporal, occipital, and prefrontal areas	Visual temporal, occipital, and prefrontal areas
García-Cabezas and Barbas (2017)	Mesocortical prefrontal areas	Mesocortical prefrontal areas
Beul et al. (2017)	Temporal, occipital, parietal, and frontal areas	Temporal, occipital, parietal, and frontal areas
Hilgetag et al. (2019)	Temporal, occipital, parietal, and frontal areas	Temporal, occipital, parietal, and frontal areas
Joyce and Barbas (2018)	Mesocortical prefrontal area 25	Entire cerebral cortex
Bautista et al. (2023)	Meso- and isocortical areas	Temporal cortex
Aparicio-Rodríguez & García-Cabezas (2023)	Selected temporal, occipital, parietal, and frontal areas	Entire cerebral cortex
Medalla and Barbas (2014)	Theoretical review	
Barbas (2015)	Theoretical review	
Barbas et al. (2018)	Theoretical review	
García-Cabezas et al. (2019)	Theoretical review	
García-Cabezas and Zikopoulos (2019)	Theoretical review	
Barbas and Hilgetag (2023)	Theoretical review	

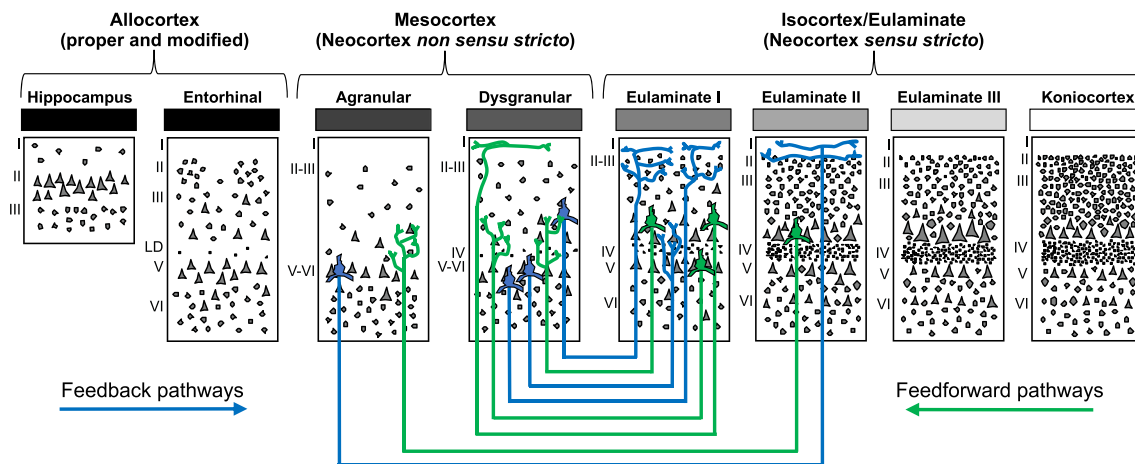
between laminar architecture and laminar patterns of synaptic cortico-cortical connection was first proposed by Helen Barbas in a seminal article (Barbas, 1986). This author further formalized this relation in the Structural Model for Cortico-cortical Connections (Barbas & Rempel-Clover, 1997). Since then, the principles of the Structural Model have been confirmed in several synaptic tract-tracing studies of macaque occipital, parietal, prefrontal, and temporal areas (Aparicio-Rodríguez & García-Cabezas, 2023; Barbas, 1986; Barbas, 2015; Barbas & Rempel-Clover, 1997; Barbas et al., 2018; Barbas & Hilgetag, 2023; Bautista et al., 2023; Beul et al., 2017; García-Cabezas & Barbas, 2017; García-Cabezas & Zikopoulos, 2019; García-Cabezas et al., 2019; Hilgetag et al., 2016; Hilgetag et al., 2019; Joyce & Barbas, 2018; Medalla & Barbas, 2006, 2014; Rempel-Clover & Barbas, 2000; see Table 2). Even more, the Structural Model has showed better capacity to predict laminar patterns of cortico-cortical connections across the entire cerebral cortex than other models of cortical connectivity (Aparicio-Rodríguez & García-Cabezas, 2023; Beul et al., 2017).

The principles of the Structural Model are represented in Figure 2a. Laminar patterns are related to the flow of information across the cerebral cortex and, thus, with cortical hierarchies (Chanes & Barrett, 2016; Felleman & Van Essen, 1991; Hilgetag & Goulas, 2020). Accordingly, pathways from areas of simpler to areas of more complex type are feedback (blue in Figure 2a) and pathways from areas of more complex to areas of simpler type are feedforward (green in Figure 2a); pathways connecting areas of comparable laminar complexity are lateral. Therefore, cortical areas of simpler types are higher in cortical hierarchies than areas of more complex types.

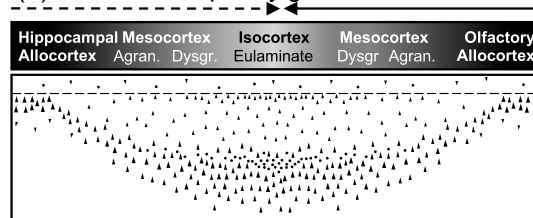
### 3.2 | Origin of primate cortical types: The Hypothesis on the Dual Origin of the Neocortex

Comparative cytoarchitectonic studies show that the primate cortical surface is not merely expanded by the addition of more cortical columns with a laminar composition comparable to that of cortical columns in rodents (García-Cabezas et al., 2019; Ruiz-Cabrera et al., 2023). The cortical types identified in the rat cerebral cortex are of simple laminar architecture (Figure 2b); in the primate cortex there are cortical types of comparable complexity to those identified in rats, but also other types of higher laminar complexity (Figure 2c) that are absent in the rat cortex. These more complex types in human embryos have more embryonic layers and intermediate precursors than the simpler types (Barbas & García-Cabezas, 2016). Thus, from a comparative point of view, the cortical gradient of progressive laminar complexity is expanded both quantitative and qualitatively in primates compared to rodents. The first attempt to explain the phylogenetic emergence of the “younger” primate cortical types was the Hypothesis on the Dual Origin of the Neocortex proposed by Friedrich Sanides (1962, 1970). Sanides traced the tangential expansion of the human cerebral cortex to two ancestral anlagen in the allocortex, the ancestral olfactory and the ancestral hippocampal cortex, which formed a continuous ring at the edge of each brain hemisphere. These anlagen gave rise to two paraolfactory and parahippocampal cytoarchitectonic trends or gradients of neocortex (Figure 2d and e). According to Sanides, mesocortical types expanded from rodents to primates in successive concentric rings that developed inside the outer allocortical ring. Thus, the isocortex appeared as an island surrounded

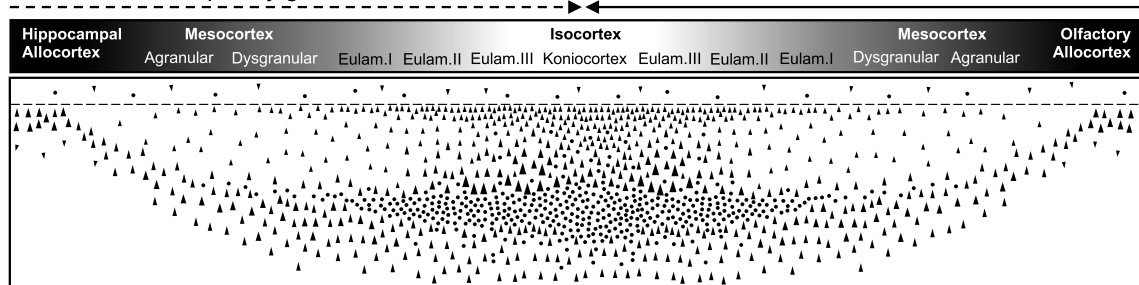
## (a) The Structural Model for Cortico-cortical Connections



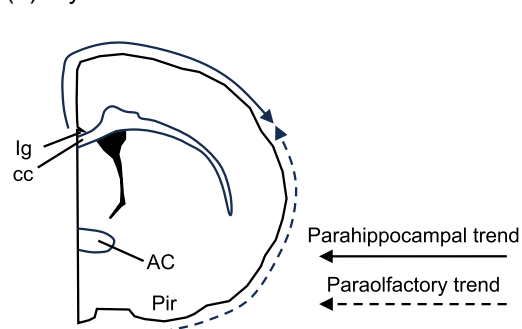
## (b) Laminar complexity gradient in the rat cortex



## (c) Laminar complexity gradient in the human cortex



## (d) Cytoarchitectonic trends in the rat cortex



## (e) Cytoarchitectonic trends in the human cortex

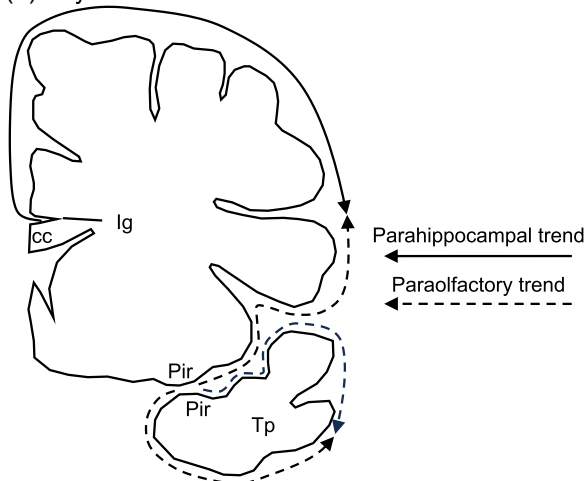


**FIGURE 2** The Structural Model for Cortico-cortical Connections and the Hypothesis on the Dual Origin of the Neocortex. (a) Principles of the Structural Model that relate laminar patterns of synaptic connections and laminar architecture of the connected areas. Pathways from areas of simpler to areas of more complex type are originated preferentially in infragranular (V–VI) layers and terminate in superficial (I–III) layers (blue neurons); these pathways are feedback. Pathways from areas of more complex to areas of simpler type are originated preferentially in supragranular (II–III) layers and terminate in middle-deep (IV–VI) layers (green neurons); these pathways are feedforward. (b) Laminar complexity

(Continues)



**FIGURE 2** (Continued)

gradient in the rat cortex; this scheme shows the increase in laminar complexity from the hippocampal and olfactory allocortex to the isocortex; the grayscale represents laminar complexity (black: simplest cortical type; lightest gray: most complex type). (c) Laminar complexity gradient in the human cortex; this scheme shows the increase in laminar complexity from the hippocampal and olfactory allocortex to the koniocortex; the grayscale represents laminar complexity (black: simplest cortical type; white: most complex type); note that in rats the primary sensory areas are not koniocortical. (d) Cytoarchitectonic trends in the rat cortex; scheme of a coronal rat brain section through the anterior commissure (AC); the parahippocampal trend (solid arrow) is originated in the hippocampal allocortex, including the Indusium griseum (Ig); the paraolfactory trend (dashed arrow) is originated in the olfactory allocortex, including the piriform cortex (Pir). (e) Cytoarchitectonic trends in the human cortex; scheme of a coronal human brain section through the temporal pole (Tp); the parahippocampal trend (solid arrow) is originated in the hippocampal allocortex, including the Indusium griseum (Ig); the paraolfactory trend (dashed arrow) is originated in the olfactory allocortex, including the piriform cortex (Pir). Parts b and c are modified from figures 3 and 4 in Ruiz-Cabrera et al. (2023). AC, anterior commissure; Agran., agranular; Dysgr., dysgranular; cc, corpus callosum; Eulam., eulaminar; Ig, Indusium griseum; Pir, piriform cortex.

by the mesocortical ring. The most ancestral allocortical and mesocortical types are identified in all mammals but koniocortical areas, the last stage of laminar complexity that emerged in evolution in the isocortical island, were identified exclusively in primates surrounded by all the other types (Sanides, 1962, 1970). It is important to note that contemporary developmental biology data supports the concentric organization of cortical types advanced by Sanides (Puelles et al., 2019) and hypothetical maps of primate cortical patterning have been proposed in the frame of this hypothesis (García-Cabezas et al., 2023a).

In summary, according to the Hypothesis on the Dual Origin of the Neocortex, the degree of laminar complexity in a given part of the primate cerebral cortex is related to its phylogenetic antiquity: areas of more complex laminar architecture appeared later in evolution than areas of simpler laminar architecture.

### 3.3 | Cortical type gradation in the human temporal lobe: From allo- to koniocortex

In previous publications, we have explained the conceptual value of cortical type for human studies and how to identify cortical types in human brain Nissl-stained sections (García-Cabezas et al., 2020; Sancha-Velasco et al., 2023). Cytoarchitectonic gradients are traced on these sections by examination under the optical microscope. The number and complexity of cortical layers that run parallel to the surface of the brain vary gradually across gradients of progressive laminar complexification. In previous studies we have defined two mesocortical (neocortex *non sensu stricto*) and four isocortical or eulaminar (neocortex *sensu stricto*) types in the human cerebral cortex (García-Cabezas et al., 2020; Sancha-Velasco et al., 2023). In the present study, we parcellated two allocortical, two mesocortical, and four isocortical types in the human temporal lobe (Figure 3). We briefly describe each of these types below.

There are two major allocortical formations in the human temporal lobe: the primary olfactory cortex (Figure 3a) and the hippocampal formation; in the latter several areas are identified from medial to lateral: fascia dentata, cornu ammonis, subiculum, presubiculum, parasubiculum, and the entorhinal cortex (Insausti et al., 2010; see also figure 12.5 in Nieuwenhuys et al., 2008). Primary olfactory areas, the fascia dentata, the cornu ammonis, and the subiculum show simple lam-

inar architecture with two or three layers (García-Cabezas & Barbas, 2014b; Gonzalez-Arny et al., 2024). The presubiculum, parasubiculum, and entorhinal cortex are adjacent to the hippocampal subiculum and have more complex laminar architecture with five or six layers (Figure 3b); contemporary genoarchitectonic analysis in mammalian embryos showed that all the hippocampal formation areas, from the fascia dentata to the entorhinal cortex, are specified within the Medial Pallium (Puelles et al., 2019); thus we consider the fascia dentata, the cornu ammonis, and the subiculum as “proper allocortex” and the presubiculum, the parasubiculum, and the entorhinal cortex as “modified allocortex” (Puelles et al., 2019).

The temporal mesocortex (or neocortex *non sensu stricto*) includes areas that either lack (agranular; Figure 3c) or have rudimentary (dysgranular; Figure 3d) layer IV; these areas have more prominent infragranular layers and their largest neuron bodies are in layer V. In the temporal lobe, there are also isocortical (also called eulaminar or neocortex *sensu stricto*) areas that have well-developed layer IV (Figure 3e–h). Eulaminar I areas have equally prominent supra- and infragranular layers and their largest pyramidal neuron bodies are in layers III and V (Figure 3e). Eulaminar II areas have more prominent supragranular layers, their largest pyramidal neuron bodies are in layer III, and have thicker layer IV than eulaminar I areas (Figure 3f). Eulaminar III areas have more prominent supragranular layers, thicker layer IV, and some quite large pyramidal neuron bodies in layer III (Figure 3g). Finally, koniocortical areas have dense supragranular layers and the thickest layer IV (Figure 3h).

Cortical type analysis in the human temporal cortex is key for applying the principles of the Structural Model. For instance, according to such principles, pathways from dysgranular areas should target the superficial layers of eulaminar I areas (Figure 2a) and pathways from eulaminar I areas should target the superficial layers of eulaminar II areas.

### 3.4 | Postmortem Braak staging

We examined four coronal temporal lobe sections (temporal pole, amygdala, anterior hippocampus, posterior hippocampus) immunostained with the antibody AT8 from eight postmortem human brains (Table 1) to stage tau pathology according to the criteria of Braak et al. (2006). This staging system is based on the presence of neurofibril-

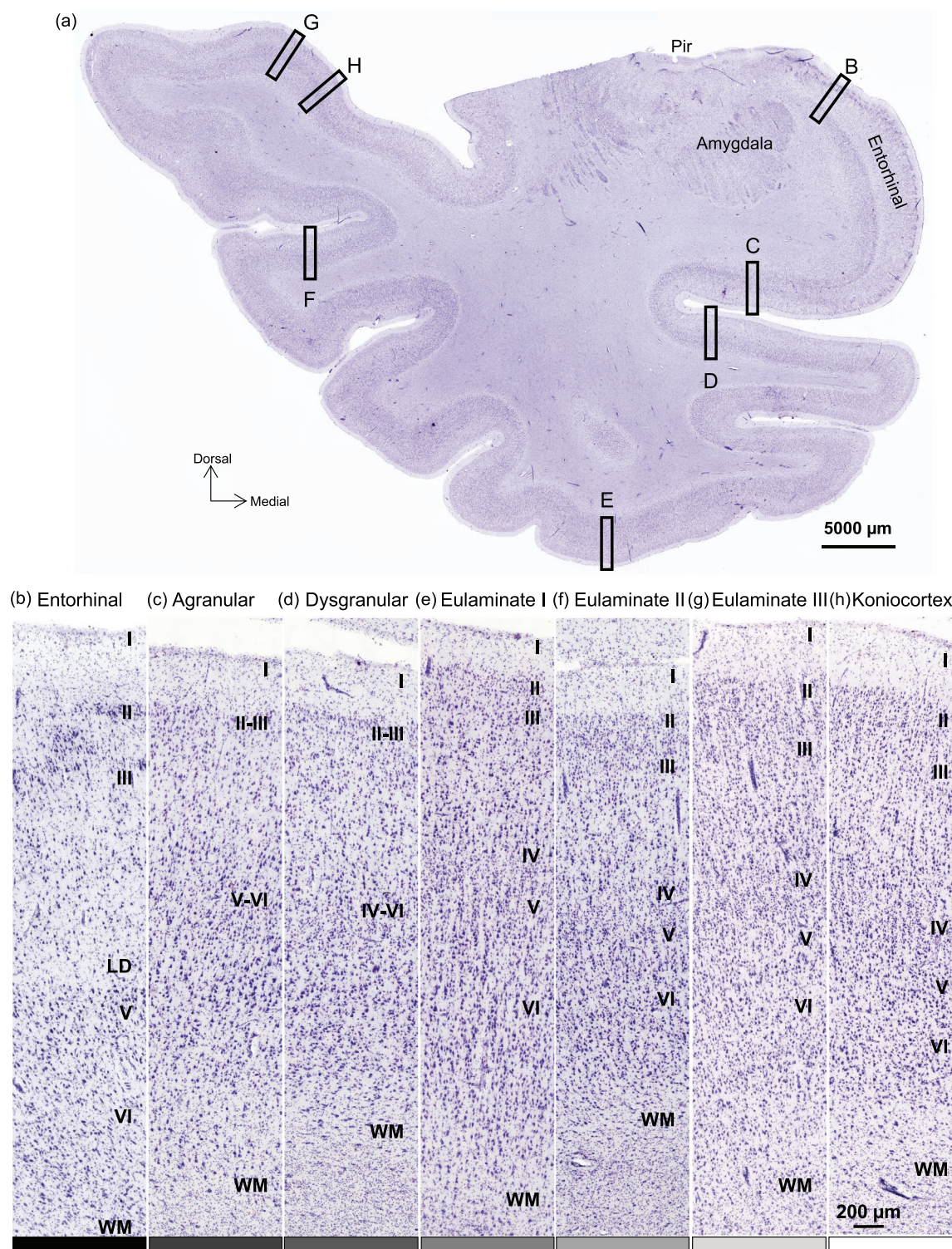


**FIGURE 3** Cortical type gradient in the human temporal cortex. (a) Low power micrograph of a human temporal lobe section (brain BCM 261) through the amygdala and the piriform (Pir) cortex stained with Nissl technique. (b, c, d, e, f, g, h) Higher power micrographs of the b, c, d, e, f, g, and h insets in a showing representative cortical columns of the entorhinal cortex and the agranular, dysgranular, eulaminate I, eulaminate II, eulaminate III, and koniocortical types, respectively. The grayscale below b, c, d, e, f, g, and h indicates the cortical type as in Figures 1c and 2c. Roman numerals indicate cortical layers. LD, lamina dissecans; WM, white matter. Calibration bar in h applies to b-h.



lary tangles and neuropil treads stained with the monoclonal antibody AT8 which labels hyperphosphorylated tau (Braak et al., 2006). Briefly, in stage I there are AT8-immunoreactive (AT8-ir) neurofibrillary tangles and neuropil treads in the transentorhinal region forming a band in layer II that can be recognized without microscopic examination (see figure 3 in Braak et al., 2006). In stage II, AT8 immunostaining is visible in the transentorhinal, entorhinal, and hippocampal regions. Stage III is characterized by the extension of AT8 immunostaining to the neocortical regions adjacent to the transentorhinal cortex. In stage IV, there is AT8 immunostaining in the inferior and middle temporal gyri. In stage V, AT8 immunostaining extends to the superior temporal gyrus and, finally, in stage VI, there is AT8 immunostaining in the primary auditory cortex (Heschel's gyrus). In some brains studied in the present article the neurofibrillary tangles and neuropil treads labeled by AT8 could not be identified without microscopic examination; these brains were staged as pre-Braak.

The pre-Braak and Braak stages of the brains analyzed in the present article are summarized in Table 1.

### 3.5 | Hyperphosphorylated tau is present in allo-, meso-, and isocortical areas in the pre-Braak stage

We found AT8-ir neurons and neuropil threads in the three brains staged as pre-Braak (Table 1), whose donors were not diagnosed of dementia. In these brains, the AT8 immunostaining, including neurons and neuropil treads, had to be detected under optical microscope examination. We counted nine AT8-ir neurons in the 30-year-old pre-Braak brain (11/F/30), 198 in the 46-year-old pre-Braak brain (BCM 261), and 189 in the 58-year-old pre-Braak brain (21/M/58). In the brain from the youngest brain donor (11/F/30), there were two AT8-ir neurons in the supragranular layers of the agranular type, one in the supragranular layers of the dysgranular type, three in the infragranular layers of the eulaminate I type, and two in the infragranular layers of the eulaminate II type; there was also one AT8-ir neuron in the superficial layers of the entorhinal cortex. In the other two pre-Braak brains, AT8-ir neurons were distributed in allocortical (proper and modified), mesocortical, and eulaminate types with some few AT8-ir neurons in the amygdala (brain BCM 261, Figure 4a–j; brain 21/M/58, Figure 5a–f). In the three pre-Braak brains, there were two patterns of AT8-ir neurons. In the first pattern, the bodies and proximal dendrites of some neurons were filled with lightly labeled granules (Figure 4e–g; arrowheads point at dendrites); sometimes, the axon was also filled with AT8-ir granules (arrow in Figure 4g). These lightly labeled neurons were surrounded by unstained neuropil. Second, some densely labeled AT8-ir neuropil treads seemed to emanate from a single unlabeled neuron body like if they corresponded to proximal and distal dendritic segments (arrowheads in Figure 4h). Some densely labeled AT8-ir neurons also had densely stained dendritic segments (arrowheads in Figure 4i) at more than 100  $\mu$ m from the neuron body; the AT8 immunostaining in the bodies of these neurons was dense (Figure 4i and j).

The number of AT8-ir neurons increased in the elder pre-Braak brains compared to the youngest of these brains. The highest increase in AT8-ir neurons was in the superficial layers of the entorhinal cortex (Figure 5e). Overall, AT8-ir neurons increased in the proper and modified allocortical areas twice than in meso- and isocortical areas (Figure 5f). We also show the overall AT8 immunostaining in the temporal lobe from one pre-Braak brain (BCM 261) for comparison with the brains with Braak stages. The pre-Braak brain BCM 261 had scant AT8-ir neuropil treads and some AT8-ir neurons in the entorhinal cortex (Figure 6a) and the mesocortical (agranular and dysgranular) types (Figure 6b and c). Scant AT8-ir neuropil treads and few rare neurons were also present in the eulaminate I and II types (Figure 6d and e). AT8 immunostaining was absent in the eulaminate III and koniocortical types (Figure 6f and g).

### 3.6 | AT8 immunostaining increases from allo- to isocortices in parallel to Braak stage progression: Qualitative description

Below, we briefly describe the AT8 immunostaining across all the cortical types of the temporal lobe in each Braak stage. In the Braak I brain, there were more AT8-ir neuropil treads and neurons in the entorhinal cortex and the agranular type (Figure 6h and i) compared to the same types in the pre-Braak brains. AT8 immunostaining, including neurons and neuropil, was most abundant in the dysgranular type (Figure 6j). In the eulaminate I type (Figure 6k), AT8 immunostaining was less abundant than in the dysgranular type, but denser than in the agranular type. Scant AT8-ir neurons and neuropil treads were identified in the eulaminate II and III types (Figure 6l and m). AT8 immunostaining was absent in the koniocortical type (Figure 6n).

In the Braak II brain, there was moderate to dense neuropil AT8 immunostaining with abundant AT8-ir neurons in the entorhinal cortex and the mesocortical (agranular and dysgranular) types (Figure 7a–c). The neuropil in the eulaminate I and II types was moderately stained and there were some AT8-ir neurons (Figure 7d and e). In the eulaminate III type, there were scant AT8-ir neuropil treads and neurons (Figure 7f). AT8 immunostaining was absent in the koniocortical type (Figure 7g). Interestingly, AT8 immunostaining in layer IV of the dysgranular, eulaminate I, and eulaminate II types was lighter than in supra- and infragranular layers.

The Braak IV brain had moderate AT8 immunostaining in the neuropil of the entorhinal cortex with abundant AT8-ir neurons (Figure 7h). In agranular, dysgranular, and eulaminate I types, there was dense AT8 immunostaining in the neuropil and abundant AT8-ir neurons (Figure 7i–k). The neuropil was moderately stained in the eulaminate II type (Figure 7l) and lightly stained in the eulaminate III type with some AT8-ir neurons (Figure 7m). In the koniocortical type there were scant AT8-ir neuropil treads (Figure 7n). In this stage, AT8 immunohistochemistry also stained neuritic plaques in all the affected types. As noted for the Braak II brain, the AT8

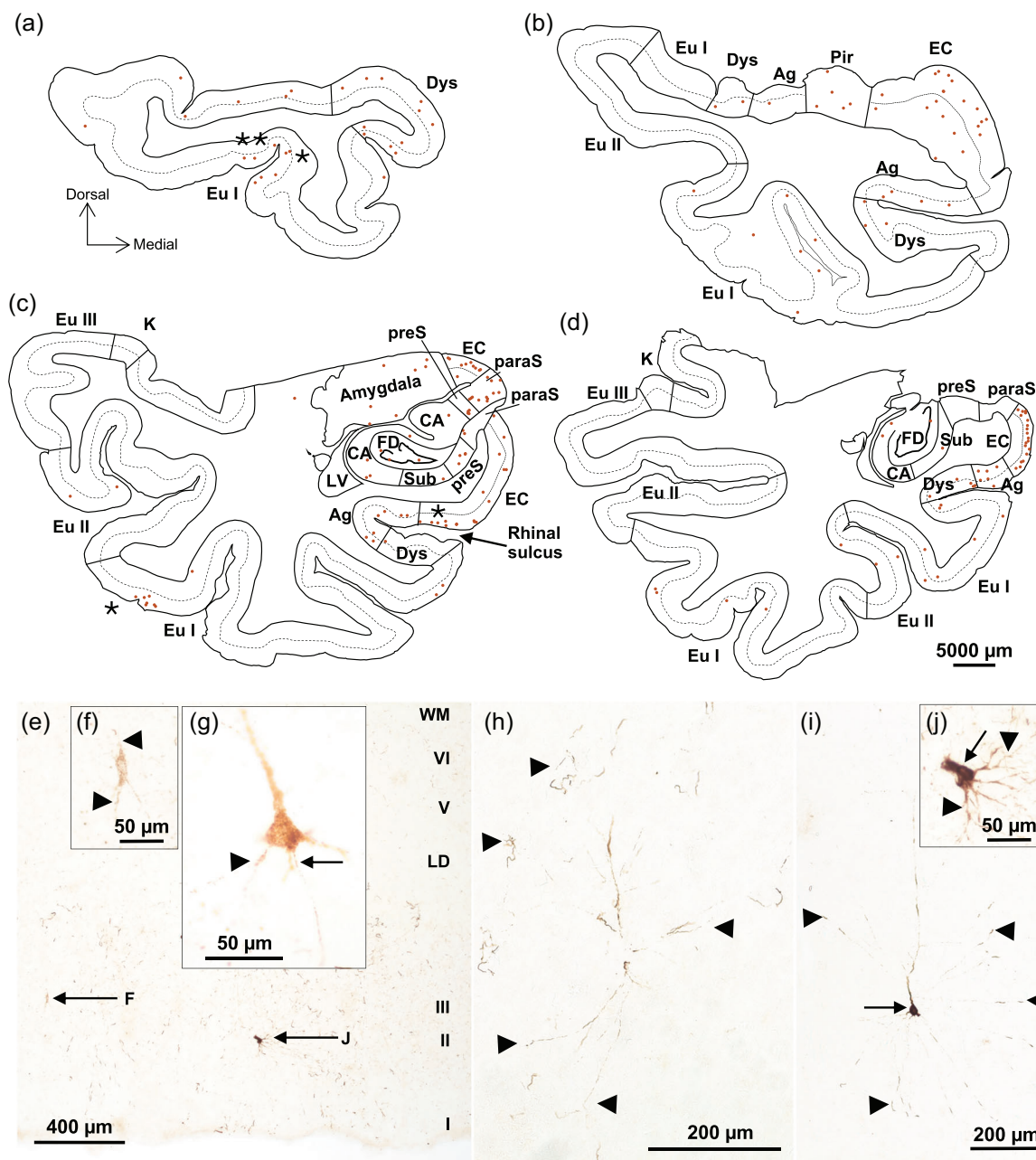


**FIGURE 4** Hyperphosphorylated tau in pre-Braak brain BCM 261. (a, b, c, d) Maps showing the distribution of AT8-ir neurons in coronal sections at the level of the temporal pole (a), the amygdala (b), the anterior (c), and the posterior hippocampus (d). Each brown dot indicates one AT8-immunoreactive (AT8-ir) neuron; the dotted lines indicate the lamina dissecans in the entorhinal cortex; the dashed lines indicate the limit between layers III and V in the agranular and dysgranular types and the upper limit of layer IV in the isocortical types. (e) Low power micrograph of the entorhinal cortex from the AT8-immunostained section mapped in c; the asterisk in c indicates the place where the micrograph was taken; arrows indicate AT8-ir neurons magnified in f and j. (f, g) Lightly labeled AT8-ir neurons from the entorhinal cortex (f in e) and the eulamine I type (g, indicated by asterisk in a); arrowheads point at labeled dendrites; the arrow in g indicates the initial segment of the axon, which contains lightly AT8 labeled granules. (h) Darkly labeled AT8-ir neuropil threads disposed concentrically around a potential unlabeled neuron body; this micrograph was taken in the eulamine I type of section in c (asterisk). (i, j) Darkly labeled neurons from the eulamine I type (i, indicated by two asterisks in a) and the entorhinal cortex (j in e); the arrows indicate the darkly labeled neuron bodies; the arrowheads indicate AT8-ir dendrites. Calibration bar in d applies to a–d. Roman numerals indicate layers of the entorhinal cortex. Ag, agranular type; CA, cornu amonis; Dys, dysgranular type; EC, entorhinal cortex; Eu I, eulamine I type; Eu II, eulamine II type; Eu III, eulamine III type; FD, fascia dentata; K, koniocortex; LD, lamina dissecans of the entorhinal cortex; LV, lateral ventricle; Pir, piriform cortex; paraS, parasubiculum; preS, presubiculum; Sub, subiculum.



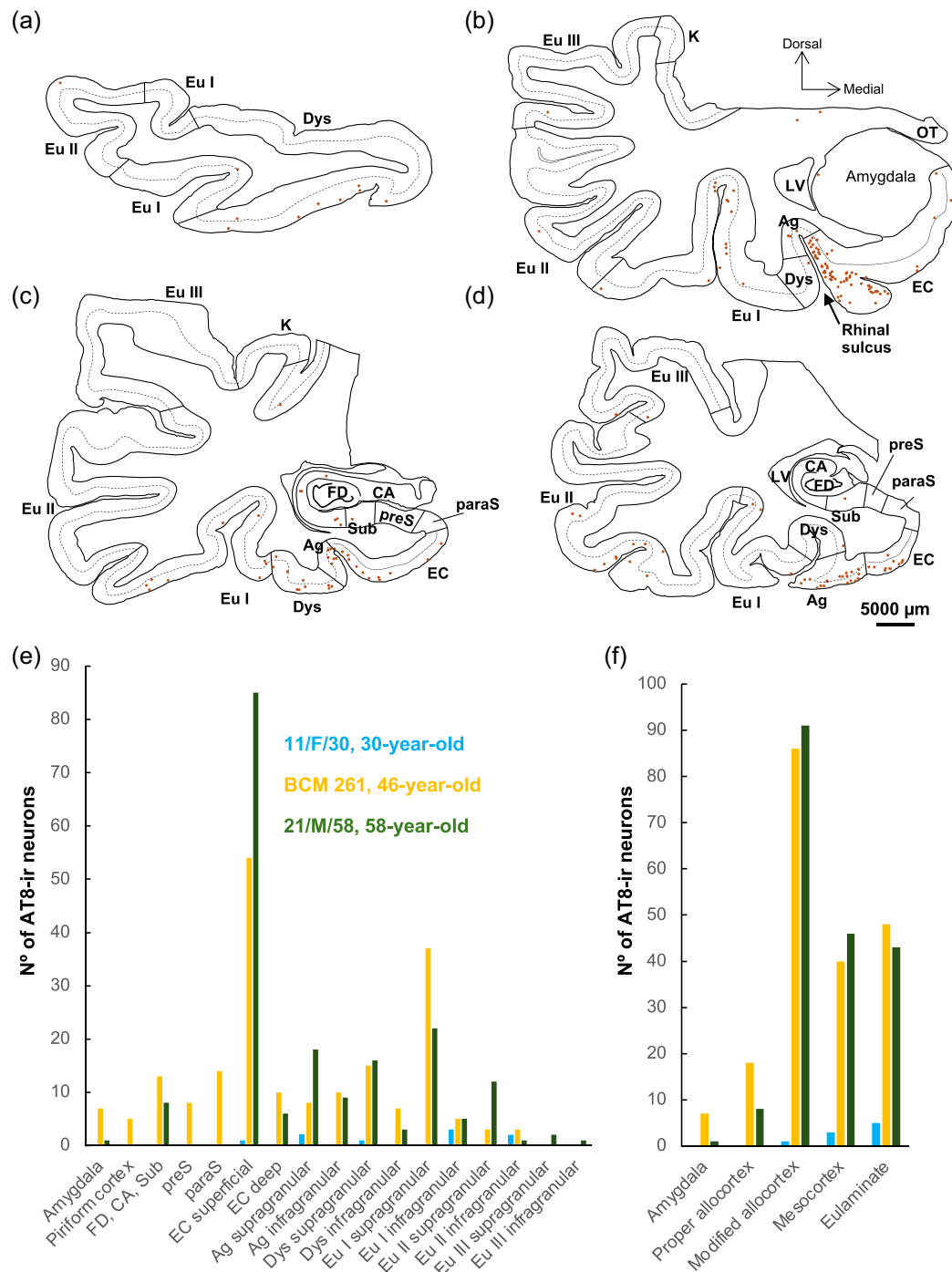


**FIGURE 5** Hyperphosphorylated tau in pre-Braak brain 21/M/58. (a, b, c, d) Maps showing the distribution of AT8-ir neurons in coronal sections of brain 21/M/58 at the level of the temporal pole (a), the amygdala (b), the anterior (c), and the posterior hippocampus (d). Each brown dot indicates one AT8-immunoreactive (AT8-ir) neuron; the dotted lines indicate the lamina dissecans in the entorhinal cortex; the dashed lines indicate the limit between layers III and V in the agranular and dysgranular types and the upper limit of layer IV in the isocortical types. (e, f) Quantification of AT8-ir labeled neurons in the three pre-Braak brains; blue: brain 11/F/30, 30-year-old; orange: brain BCM 261, 46-year-old; green: brain 21/M/58, 58-year-old. Calibration bar in d applies to a–d. Ag, agranular type; CA, cornu ammonis; Dys, dysgranular type; EC, entorhinal cortex; Eu I, eulaminar I type; Eu II, eulaminar II type; Eu III, eulaminar III type; FD, fascia dentata; K, koniocortex; LV, lateral ventricle; OT, optic tract; paraS, parasubiculum; preS, presubiculum; Sub, subiculum.

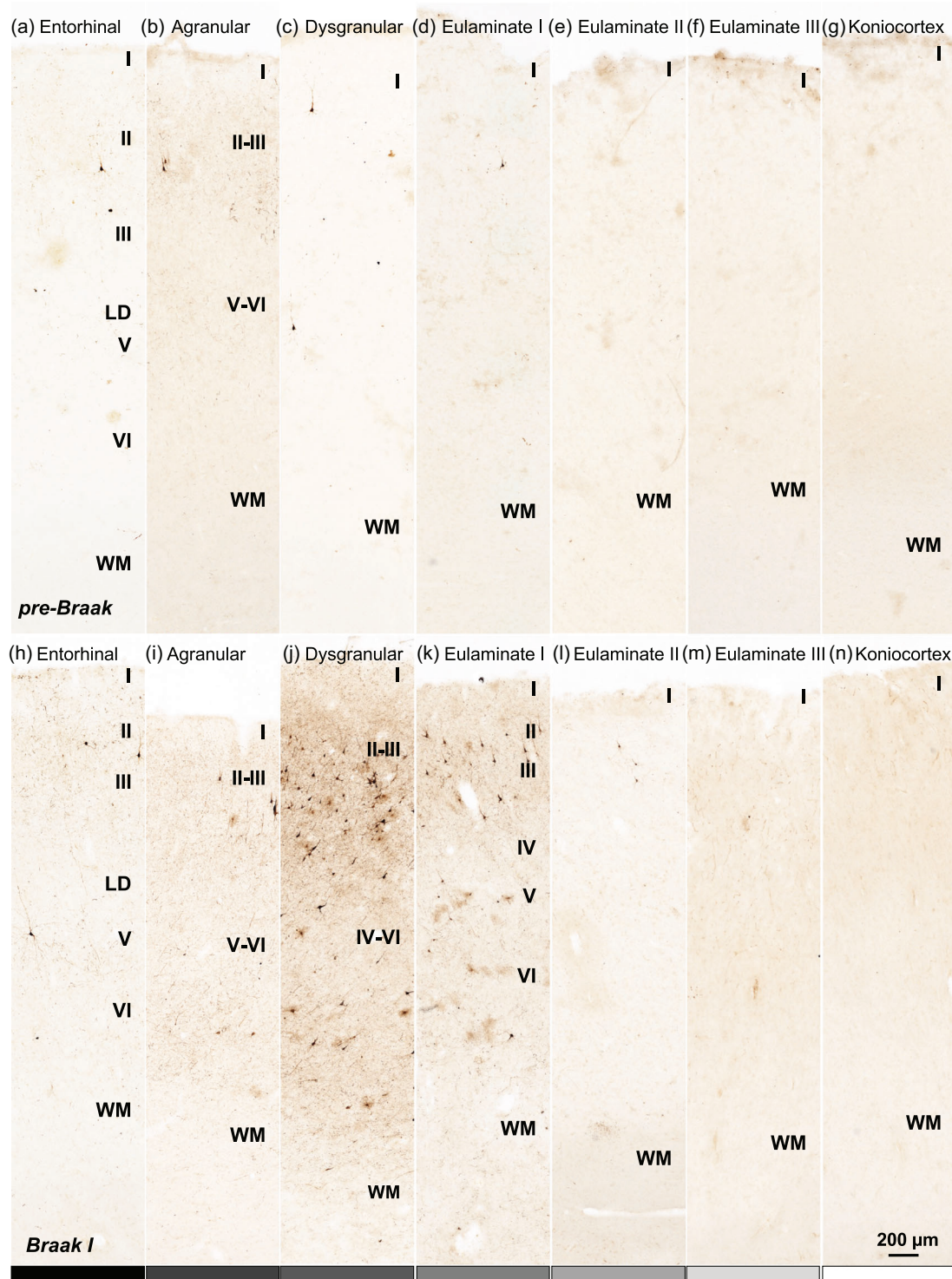


**FIGURE 6** Hyperphosphorylated tau spreading along the temporal cortex in early Braak stages. (a, b, c, d, e, f, g) Higher power micrographs from temporal lobe sections of brain BCM 261 (pre-Braak stage) stained for the monoclonal AT8 antibody that labels hyperphosphorylated tau showing representative cortical columns of the entorhinal cortex (modified allocortex) and the agranular, dysgranular, eulamine I, eulamine II, eulamine III, and koniocortical types, respectively. In the entorhinal cortex (a) and the agranular type (b), there are some AT8-immunoreactive (AT8-ir) neurons and neuropil treads. AT8 immunostaining is scant in the dysgranular (c), and eulamine (d–f) types, and is absent in the koniocortex (g). (h, i, j, k, l, m, n) Higher power micrographs from temporal lobe sections of brain 28/M/67 (Braak I stage) stained for the monoclonal AT8 antibody that labels hyperphosphorylated tau showing representative cortical columns of the entorhinal cortex (modified allocortex) and the agranular, dysgranular, eulamine I, eulamine II, eulamine III, and koniocortical types, respectively. In the entorhinal (h) and agranular types (i), there are some AT8-immunoreactive (AT8-ir) neurons and neuropil treads. In the dysgranular type (j), there is moderate AT8 immunostaining in the neuropil of supra- and infragranular layers and abundant darkly AT8-ir neurons. AT8 immunostaining and -ir neurons are less abundant in the eulamine I type (k), scant in the eulamine II (l) and eulamine III (m) types, and absent in the koniocortex (n). The grayscale below h, i, j, k, l, m,

(Continues)

**FIGURE 6** (Continued)

and n also applies to a, b, c, d, e, f, and g and indicates the cortical type as in Figures 1c, 2c, and 3b–h. Roman numerals indicate cortical layers. LD, lamina dissecans; WM, white matter. Calibration bar in n applies to a–n.

**TABLE 3** Micrographic sampling for AT8 immunostaining and neuron counts.

Case	Micrographs							Neuron n°
	EC	Ag	Dys	Eu I	Eu II	Eu III	K	
11/F/30	–	–	–	–	–	–	–	9
BCM 261	–	–	–	–	–	–	–	198
21/M/58	–	–	–	–	–	–	–	189
28/M/67	2	4	4	4	–	–	–	291
BCPA 840	2	3	3	4	3	–	–	505
BCPA 1093	2	4	4	4	3	3	2	1893
BCPA 392	2	4	4	3	3	2	2	3516
BCPA 991	2	4	4	4	4	4	2	3710

Ag, agranular type; Dys, dysgranular type; EC, entorhinal cortex; Eu I, eulamine I type; Eu II, eulamine II type; Eu III, eulamine III type; K, koniocortex.

immunostaining in layer IV of the dysgranular, eulamine I, and eulamine II types was lighter than in supra- and infragranular layers.

In Braak V brains, there was dense AT8 immunostaining in the neuropil of the entorhinal cortex and the agranular, dysgranular, eulamine I, and eulamine II types with abundant AT8-ir neurons (Figure 8a–e). The neuropil in the eulamine III type was moderately stained and had some AT8-ir neurons (Figure 8f). There were also AT8-ir neurons and neuropil treads in the koniocortical type (Figure 8g). AT8 also stained neuritic plaques in all the affected types. The AT8 immunostaining in layer IV of the eulamine I, II, and III types was lighter than in the other layers.

Finally, in the Braak VI brain, there was dense AT8 immunostaining and abundant AT8-ir neurons and neuritic plaques in the neuropil of the entorhinal cortex and all the neocortical types (Figure 8h–n). Layer IV in the dysgranular, eulamine, and koniocortical types had lighter AT8 immunostaining than the other layers. It is important to note that in all the Braak staged brains there were AT8-ir neurons with the two patterns described in the pre-Braak brains: (1) lightly labeled in their bodies, proximal dendrites, and axon and (2) densely labeled from their distal dendrites to their bodies.

### 3.7 | AT8 immunostaining increases from allo- to isocortices in parallel to Braak stage progression: Optical density quantification

We also quantified optical density (OD in pixels/ $\mu\text{m}^2$ ) in micrographs of representative columns taken from the straight gyrus part of the entorhinal cortex and the neocortical types in each AT8-immunostained section. The micrographic sampling is summarized in Table 3. We quantified AT8 immunostaining OD across all (I–VI), supra-

(I–III), and infragranular (V–VI) layers; for the entorhinal cortex, we did not differentiate superficial and deep layers because this distinction does not correspond to the supra- and infragranular layers in the neocortex. The raw data of OD quantification are available in the Supporting File 1. We present these data from two points of view. First, we show AT8 immunostaining OD levels in all the cortical types within each Braak stage (Figure 9a–c; Braak I, blue; Braak II, red; Braak IV, green; Braak V, purple; Braak VI, orange); the Kolmogorov–Smirnov normality tests for each quantification data grouped by Braak stage are summarized in Table 4. Second, we show AT8 immunostaining OD levels in all the Braak stages within each cortical type [Figure 9d–f; grayscale represents laminar complexity (black: simplest cortical type; lightest gray: most complex type)]; The Kolmogorov–Smirnov normality tests for each quantification data grouped by cortical type are summarized in Table 5. In Figure 9, each dot represents the OD value for a single column tiff file.

AT8 immunostaining OD quantification showed the overall spreading pattern described qualitatively in the previous sections, with OD levels increasing from Braak I to Braak VI, with a peak in the Braak IV stage (Figure 9a). The pattern of progressive increase in AT8 immunostaining OD was more obvious for the supragranular (I–III; Figure 9b) and infragranular (V–VI; Figure 9c) layers, likely because the lightly stained layer IV was not taken into account. The highest overall (layers I–VI) AT8 immunostaining OD levels were found in the entorhinal cortex and the agranular and dysgranular types in the Braak IV and V stages (Figure 9d). The overall OD level in the entorhinal cortex increased as AD progressed, but in the mesocortical types it peaked at Braak IV stage and decreased in the most advanced stages (Figure 9d).

In the eulamine types, the overall OD level increased with AD progression (Figure 9d). The AT8 immunostaining OD level in supra- (I–III) and infragranular (V–VI) layers increased progressively in all neocortical types with AD progression, although in the mesocortical types (agranular and dysgranular), it peaked at the Braak V stage (Figure 9e



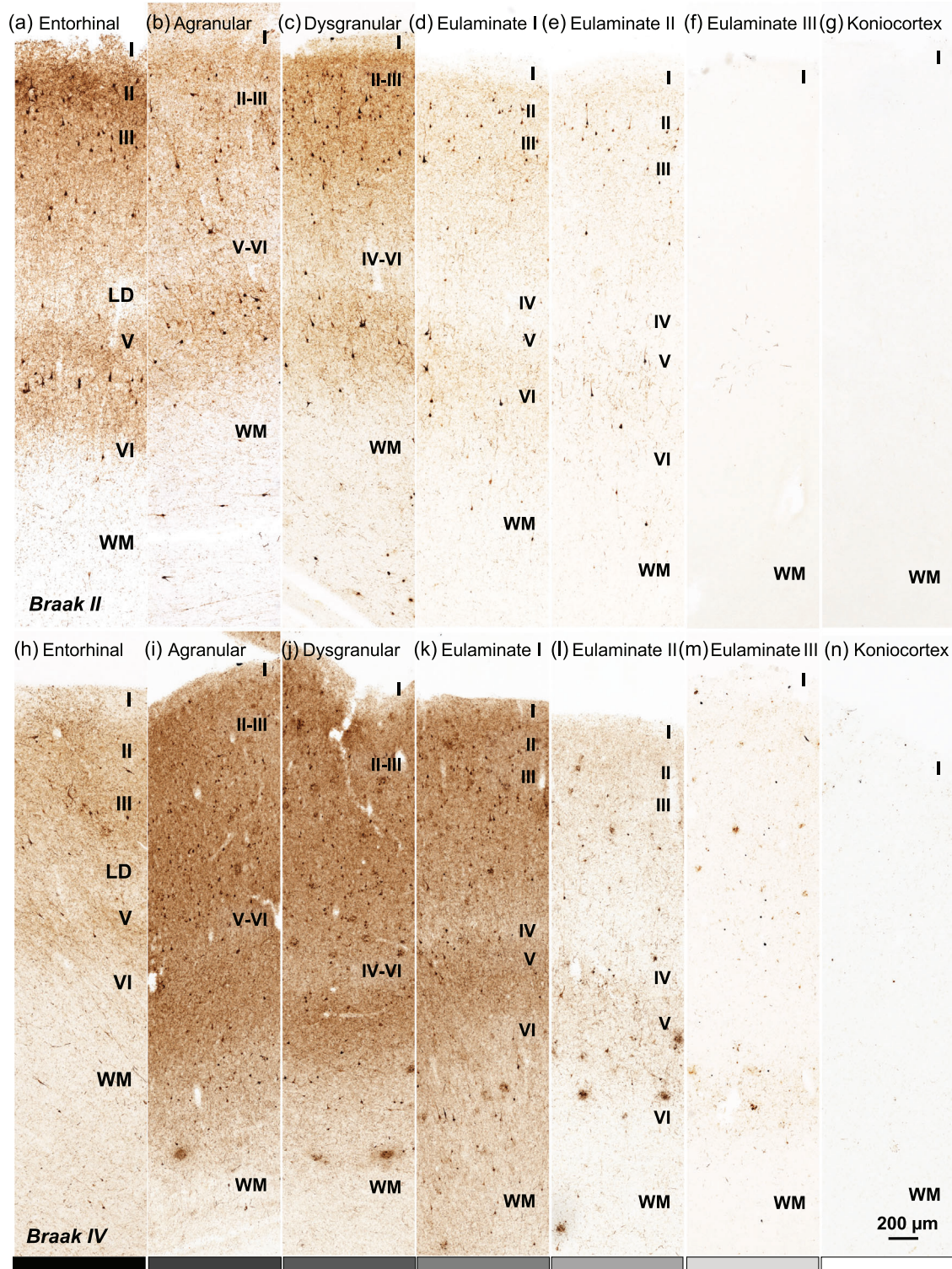


**FIGURE 7** Hyperphosphorylated tau spreading along the temporal cortex in intermediate Braak stages. (a, b, c, d, e, f, g) Higher power micrographs from temporal lobe sections of brain BCPA 840 (Braak II stage) stained for the monoclonal AT8 antibody that labels hyperphosphorylated tau showing representative cortical columns of the entorhinal cortex (modified allocortex) and the agranular, dysgranular, eulamine I, eulamine II, eulamine III, and koniocortical types, respectively. In the entorhinal cortex (a) there is mild AT8 immunostaining in the neuropil with some darkly AT8-immunoreactive (AT8-ir) neurons. In the agranular (b) and dysgranular (c) types, there is moderate AT8 immunostaining in the neuropil of supra- and infragranular layers and abundant darkly AT8-ir neurons. In the eulamine I type (d), the AT8 immunostaining in the neuropil is milder and there are fewer AT8-ir neurons. In the eulamine II type (e), AT8 immunostaining is lighter and AT8-ir neurons are scant. AT8 immunostaining is scant in the eulamine III (f) and absent in the koniocortical type (g). (h, i, j, k, l, m, n) Higher power micrographs from temporal lobe sections of brain BCPA 1093 (Braak IV stage) stained for the monoclonal AT8 antibody that labels hyperphosphorylated tau showing representative cortical columns of the entorhinal cortex (modified allocortex) and the agranular, dysgranular,

(Continues)



**FIGURE 7** (Continued)

eulaminar I, eulaminar II, eulaminar III, and koniocortical types, respectively. In the entorhinal cortex (h) there is moderate AT8 immunostaining in the neuropil with some darkly AT8-ir neurons. In the agranular (i), dysgranular (j), and eulaminar I (k) types, there is dense AT8 immunostaining in the neuropil of supra- and infragranular layers; there are also abundant darkly AT8-ir neurons and neuritic plaques. In the eulaminar II type (l), AT8 immunostaining in the neuropil is milder and there are fewer AT8-ir neurons and abundant AT8-ir neuritic plaques. AT8 immunostaining is light in the eulaminar III (m) and scant in the koniocortical (n) type. The grayscale below h, i, j, k, l, m, and n also applies to a, b, c, d, e, f, and g and indicates the cortical type as in Figures 1c, 2c, and 3b–h. Roman numerals indicate cortical layers. LD, lamina dissecans; WM, white matter. Calibration bar in n applies to a–n.

**TABLE 4** Kolmogorov–Smirnov normality tests for each quantification data grouped by Braak stage.

Variables	Braak I	Braak II	Braak IV	Braak V	Braak VI
OD (I–VI)	No ( $p < .05$ )	Yes ( $p > .05$ )	No ( $p < .05$ )	Yes ( $p > .1$ )	Yes ( $p > .1$ )
OD (Supragranular, I–III)	No ( $p < .001$ )	No ( $p < .05$ )	Yes ( $p > .1$ )	Yes ( $p > .1$ )	No ( $p < .01$ )
OD (Infragranular, V–VI)	No ( $p < .05$ )	No ( $p < .01$ )	Yes ( $p > .1$ )	Yes ( $p > .1$ )	Yes ( $p > .1$ )
AT8-ir neurons (II–III, V–VI)	No ( $p < .001$ )	No ( $p < .05$ )	Yes ( $p > .1$ )	Yes ( $p > .05$ )	No ( $p > .1$ )
AT8-ir neurons (Supragranular, II–III)	No ( $p < .01$ )	Yes ( $p > .1$ )	No ( $p < .01$ )	Yes ( $p > .1$ )	Yes ( $p > .1$ )
AT8-ir neurons (Infragranular, V–VI)	No ( $p < .01$ )	Yes ( $p > .1$ )	No ( $p < .01$ )	Yes ( $p > .1$ )	Yes ( $p > .1$ )
Fraction of supragranular AT8-ir neurons	Yes ( $p > .1$ )	Yes ( $p > .1$ )	Yes ( $p > .1$ )	Yes ( $p > .1$ )	Yes ( $p > .1$ )

Yes: Normal distribution; No: Not normal distribution.

**TABLE 5** Kolmogorov–Smirnov normality tests for each quantification data grouped by cortical type.

Variables	Entorhinal	Agranular	Dysgranular	Eulaminar I	Eulaminar II	Eulaminar III	Koniocortex
OD (I–VI)	Yes ( $p > .1$ )	Yes ( $p > .1$ )	Yes ( $p > .1$ )	No ( $p < .05$ )	Yes ( $p > .1$ )	Yes ( $p > .1$ )	No ( $p < .01$ )
OD (Supragranular, I–III)	–	No ( $p < .05$ )	Yes ( $p > .1$ )	No ( $p < .05$ )	No ( $p < .01$ )	Yes ( $p > .1$ )	No ( $p < .05$ )
OD (Infragranular, V–VI)	–	No ( $p < .05$ )	Yes ( $p > .1$ )	Yes ( $p > .1$ )	No ( $p < .01$ )	Yes ( $p > .1$ )	No ( $p < .05$ )
AT8-ir neurons (II–III, V–VI)	Yes ( $p > .1$ )	Yes ( $p > .1$ )	Yes ( $p > .1$ )	No ( $p < .05$ )	Yes ( $p > .05$ )	Yes ( $p > .1$ )	Yes ( $p > .1$ )
AT8-ir neurons (Supragranular, II–III)	–	Yes ( $p > .05$ )	Yes ( $p > .1$ )	No ( $p < .01$ )	Yes ( $p > .05$ )	Yes ( $p > .05$ )	Yes ( $p > .1$ )
AT8-ir neurons (Infragranular, V–VI)	–	Yes ( $p > .05$ )	Yes ( $p > .1$ )	No ( $p < .05$ )	Yes ( $p > .05$ )	Yes ( $p > .1$ )	Yes ( $p > .1$ )
Fraction of supragranular AT8-ir neurons	–	Yes ( $p > .1$ )	Yes ( $p > .1$ )	Yes ( $p > .1$ )	No ( $p < .05$ )	Yes ( $p > .5$ )	Yes ( $p > .1$ )

Yes: Normal distribution; No: Not normal distribution.

and f). The AT8 immunostaining OD level in supragranular (I–III) layers was higher than in infragranular layers in all the neocortical types, except for the agranular type (Figure 9e and f).

In summary, AT8 immunostaining OD levels increased in parallel to AD progression along the cortical gradient of laminar complexity, except for a decrease in the most advanced AD stages (Braak V and VI) in the mesocortical (agranular and dysgranular) types.

### 3.8 | The number of AT8-ir neurons increases from allo- to isocortices in parallel to Braak stage progression

We also quantified the AT8-ir neurons across supragranular (II–III), infragranular (V–VI), and supra- and infragranular (II–III, V–VI) layers in the same micrographs used for OD quantification (Table 3); for the

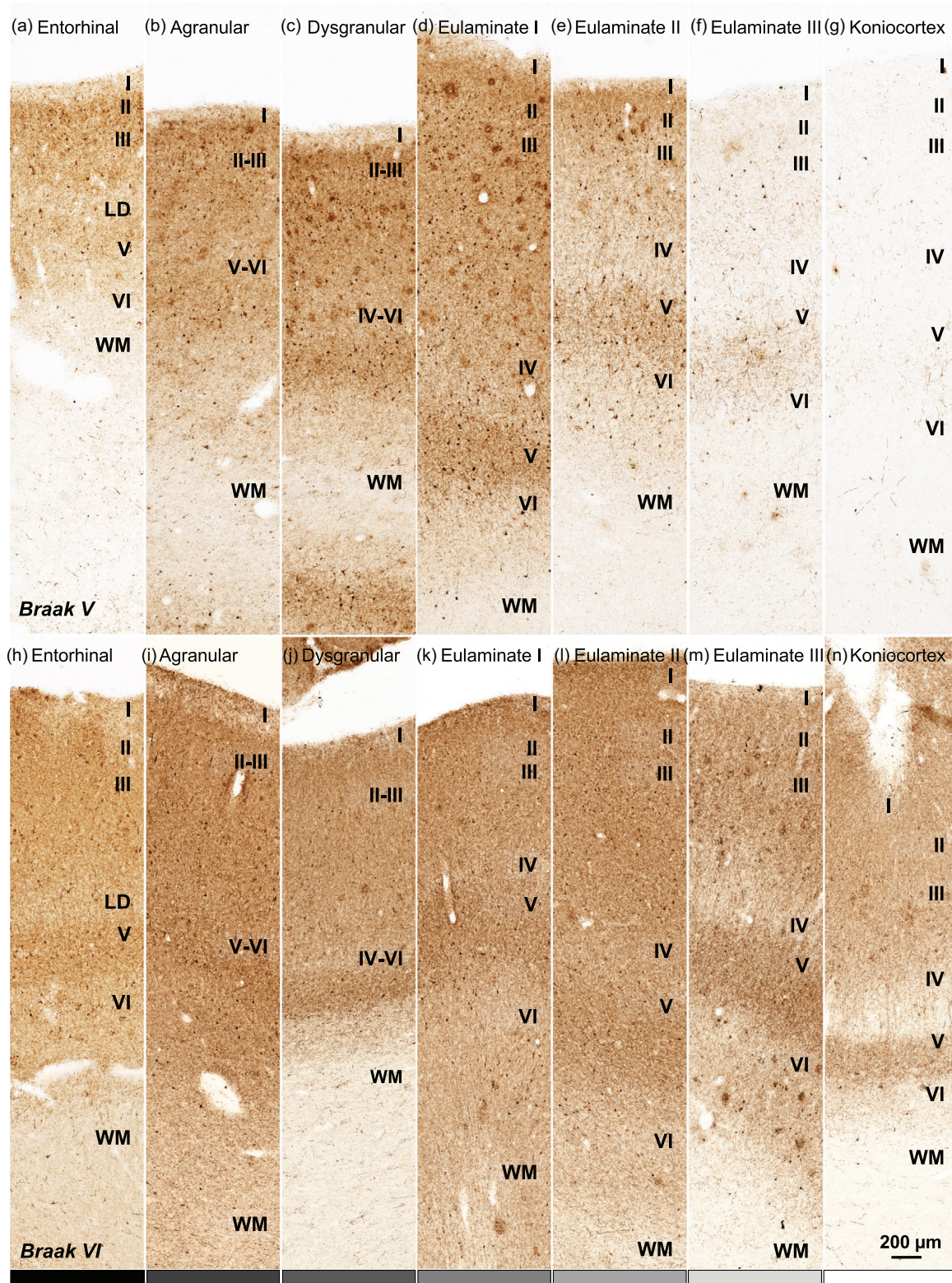


**FIGURE 8** Hyperphosphorylated tau spreading along the temporal cortex in advanced Braak stages. (a, b, c, d, e, f, g) Higher power micrographs from temporal lobe sections of brain BCPA 392 (Braak V stage) stained for the monoclonal AT8 antibody that labels hyperphosphorylated tau showing representative cortical columns of the entorhinal cortex (modified allocortex) and the agranular, dysgranular, eulamine I, eulamine II, eulamine III, and koniocortical types, respectively. In the entorhinal cortex (a) and the agranular (b), dysgranular (c), eulamine I (d), and eulamine II (e) types there is dense AT8 immunostaining in the neuropil of supra- and infragranular layers; there are also abundant darkly AT8-immunoreactive (AT8-ir) neurons and neuritic plaques. In the eulamine III type (f), there is moderate AT8 immunostaining in the neuropil of supra- and infragranular layers, abundant darkly AT8-ir neurons and some neuritic plaques. In the koniocortical type (g), there are some neuropil treads and AT8-ir neurons. (h, i, j, k, l, m, n) Higher power micrographs from temporal lobe sections of brain BCPA 991 (Braak VI

(Continues)



**FIGURE 8** (Continued)

stage) stained for the monoclonal AT8 antibody that labels hyperphosphorylated tau showing representative cortical columns of the entorhinal cortex (modified allocortex) and the agranular, dysgranular, eulamine I, eulamine II, eulamine III, and koniocortical types, respectively. There is dense AT8 immunostaining in the neuropil of supra- and infragranular layers and abundant darkly AT8-ir neurons and neuritic plaques in all the cortical types (h–n). The grayscale below h, i, j, k, l, m, and n also applies to a, b, c, d, e, f, and g and indicates the cortical type as in Figures 1c, 2c, and 3b–h. Roman numerals indicate cortical layers. LD, lamina dissecans; WM, white matter. Calibration bar in n applies to a–n.

entorhinal cortex, we did not differentiate superficial and deep layers because this distinction does not correspond to the supra- and infragranular layers in the neocortex. The raw data of AT8-ir neuron quantification are available in the Supporting File 1. We present these data from two points of view. First, we show AT8-ir neuron counts in all the cortical types within each Braak stage (Figure 10a–c; Braak I, blue; Braak II, red; Braak IV, green; Braak V, purple; Braak VI, orange); the Kolmogorov–Smirnov normality tests for each quantification data grouped by Braak stage are summarized in Table 4. Second, we show AT8-ir neuron counts in all the Braak stages within each cortical type [Figure 10d–f; grayscale represents laminar complexity (black: simplest cortical type; lightest gray: most complex type)]; the Kolmogorov–Smirnov normality tests for each quantification data grouped by cortical type are summarized in Table 5. In Figure 10, each dot represents the AT8-ir neuron count value for a single column tiff file.

In total, 10271 profiles were identified by the customized macro; of those, 623 were excluded and 267 were manually added; thus, the final number of AT8-ir neurons counted in the Braak stages brains was 9915. The total counts of AT8-ir neurons per case are summarized in Table 3. The number of AT8-ir neurons increased in parallel to AD progression with a peak in Braak V stage and a moderate decrease in Braak VI stage (Figure 10a–c).

From the point of view of cortical types, the number of AT8-ir neurons increased progressively along the entorhinal cortex and the neocortical types with a peak in the Braak V stage and a moderate decrease in the Braak VI stage in the mesocortical (agranular and dysgranular) and the eulamine I and II types; in the eulamine III and koniocortical types the number of AT8-ir neurons peaked in the Braak VI stage (Figure 10d–f). The highest AT8-ir neuron count for layers I–VI and the supragranular (II–III) layers were obtained in the mesocortical (agranular and dysgranular) types (Figure 10d and e); for the infragranular (V–VI) layers, the highest AT8-ir neuron counts were also obtained in the agranular type (Figure 10f).

In summary, the count of AT8-ir neurons increased in parallel to AD progression along the cortical gradient of laminar complexity of the temporal lobe, except for a decrease in the most advanced AD stages (Braak V and VI) in the mesocortical (agranular and dysgranular) and eulamine I and II types.

### 3.9 | Hyperphosphorylated tau advances toward the koniocortex by reaching first the supragranular layers

The qualitative and quantitative analysis of AT8 immunostaining described in the previous sections (Figures 6–10) shows that hyper-

phosphorylated tau spreads along cortical types of the temporal lobe in parallel to Braak stages. We represent this spreading across all the temporal cortical types in parallel to Braak stages as quantified by mean AT8 immunostaining OD (Figure 11a) and mean AT8-ir neuron count (Figure 11b). This representation highlights the progressive spread of hyperphosphorylated tau along temporal cortical types starting at the entorhinal cortex (modified allocortex) and the mesocortices. The eulamine III and koniocortical types are the last in being involved in hyperphosphorylated tau pathology. In the most advanced Braak stages, AT8 immunostaining and AT8-ir neurons decrease in the cortical types that had the earliest involvement, except in the entorhinal cortex where AT8-ir neurons reach their maximum count (Figure 11a and b).

It is known by synaptic tract-tracing studies in nonhuman primates that cortico-cortical connections between different cortical types show characteristic laminar patterns (Figure 2a). If hyperphosphorylated tau spreads transsynaptically, it should be expected that it would follow a laminar pattern of spreading concordant to the predictions of the Structural Model (Barbas & Rempel-Clower, 1997; García-Cabezas et al., 2019). Does hyperphosphorylated tau spread from one cortical type to another following specific laminar patterns? To answer this question, we divided AT8-ir supragranular neuron counts by the sum of AT8-ir supra- and infragranular neuron counts in each cortical type within each Braak stage to compute the fraction of AT8-ir supragranular neurons. We represent these fraction data in Figure 11c. In the dysgranular, eulamine I, and II types, there were more AT8-ir neurons in the supra- (II–III) than in the infragranular (V–VI) layers in the early Braak (I–II) stages; in the middle and advanced Braak (IV–VI) stages, the fraction of AT8-ir supragranular neurons decreased and approached the 0.5 value [equal number of AT8-ir neurons in supra- (II–III) and infragranular (V–VI) layers]. In the eulamine III and the koniocortical type, there were more AT8-ir neurons in the supra- (II–III) than in the infragranular (V–VI) layers. In the agranular type overall, there were more AT8-ir neurons in the infra- (V–VI) than in the supragranular (II–III) layers and the fraction of AT8-ir supragranular neurons tended to increase toward the 0.5 value in middle and advanced Braak (IV–VI) stages. The representation of the fraction of AT8-ir supragranular neurons across all the temporal cortical types in parallel to Braak stages shows these trends altogether (Figure 11d).

In summary, from the dysgranular to the koniocortical type hyperphosphorylated tau spreads preferentially through the supragranular layers and, as Braak stages progress, the involvement of supra- and infragranular layers tends to balance. In the agranular type, there are more AT8-ir neurons in the infra- than in the supragranular layers even in the most advanced Braak stages.

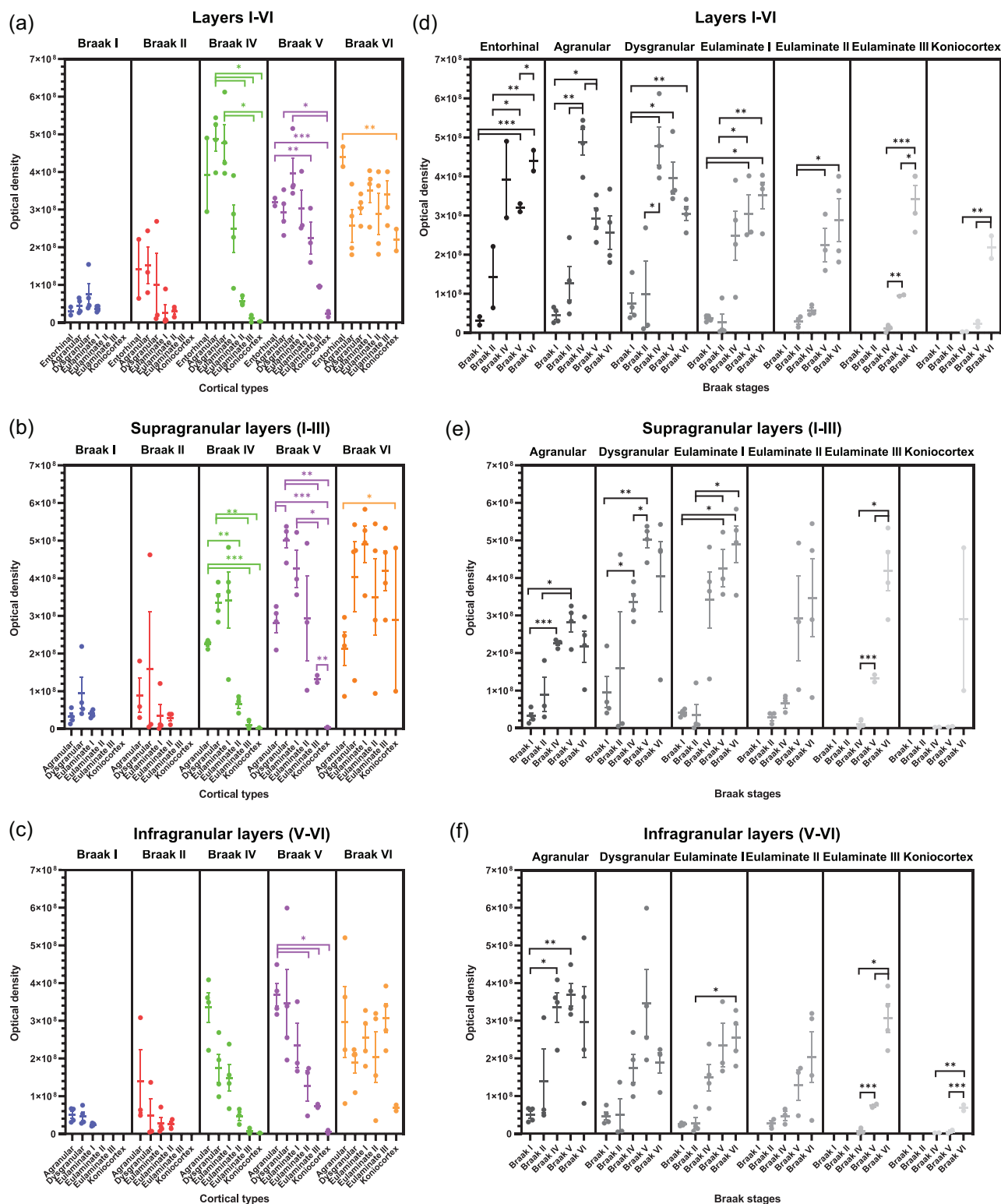


**FIGURE 9** Optical density (OD) quantification of AT8 immunostaining. (a, b, c) AT8 immunostaining OD in all the cortical types within each Braak stage (Braak I, blue; Braak II, red; Braak IV, green; Braak V, purple; Braak VI, orange) for layers I–VI (a), supragranular (I–III) layers (b), and infragranular (V–VI) layers (c); each dot represents the OD value for a single column tiff file. (d, e, f) AT8 immunostaining OD levels in all the Braak stages within each cortical type [grayscale represents laminar complexity, from black (simplest cortical type) to lightest gray (most complex type)] for layers I–VI (d), supragranular (I–III) layers (e), and infragranular (V–VI) layers (f); each dot represents the OD value for a single column tiff file. Significant differences are indicated with asterisks [ $p < .05$  (\*),  $p < .01$  (\*\*), and  $p < .001$  (\*\*\*)].



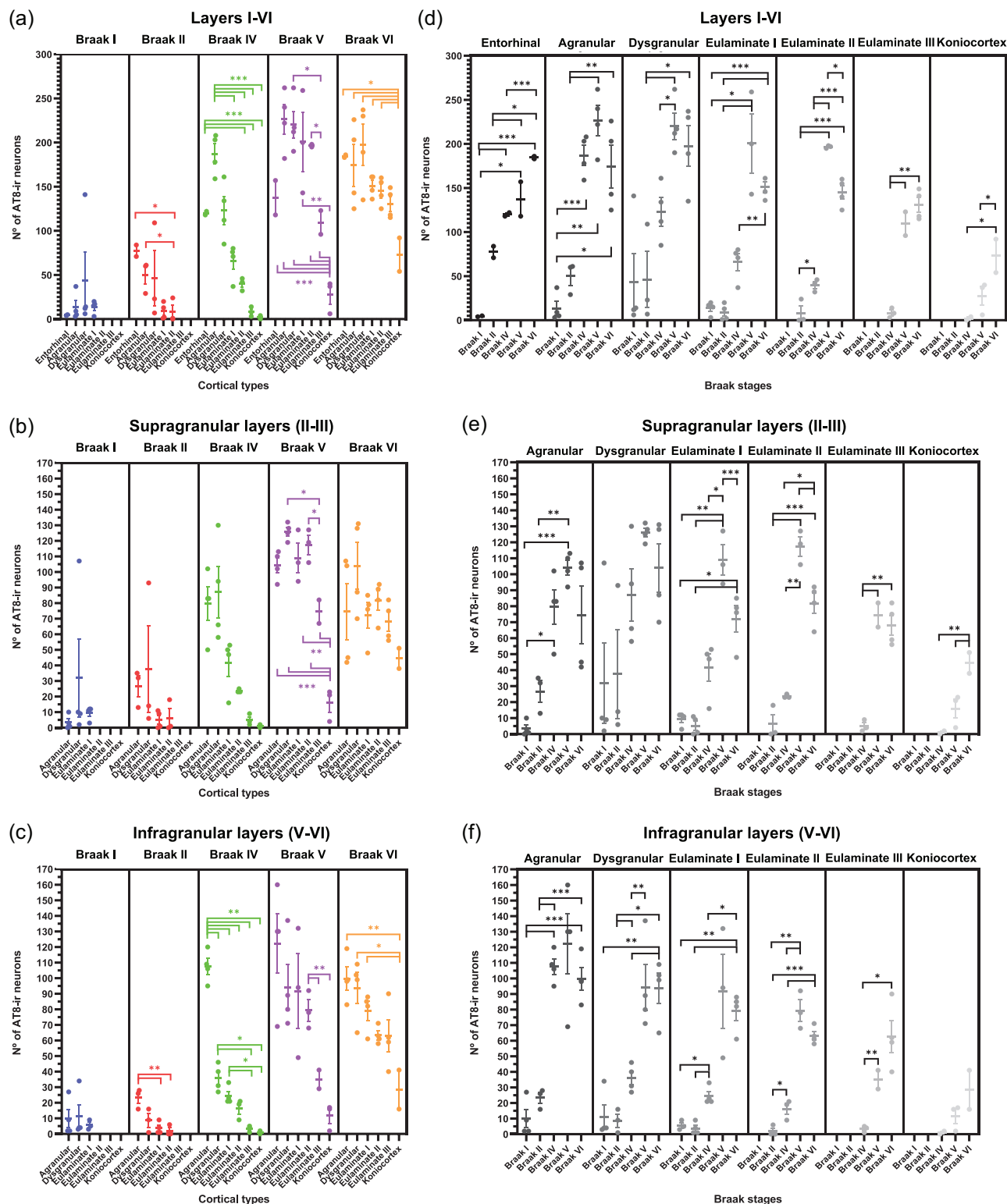


**FIGURE 10** AT8-immunoreactive (AT8-ir) neuron quantification. (a, b, c) AT8-ir neuron counts in all the cortical types within each Braak stage (Braak I, blue; Braak II, red; Braak IV, green; Braak V, purple; Braak VI, orange) for layers I–VI (a), supragranular (II–III) layers (b), and infragranular (V–VI) layers (c); each dot represents the AT8-ir neuron count for a single column tiff file. (d, e, f) AT8-ir neuron counts in all the Braak stages within each cortical type [grayscale represents laminar complexity, from black (simplest cortical type) to lightest gray (most complex type)] for layers I–VI (d), supragranular (II–III) layers (e), and infragranular (V–VI) layers (f); each dot represents the AT8-ir neuron count for a single column tiff file. Significant differences are indicated with asterisks [ $p < .05$  (\*),  $p < .01$  (\*\*), and  $p < .001$  (\*\*\*)].

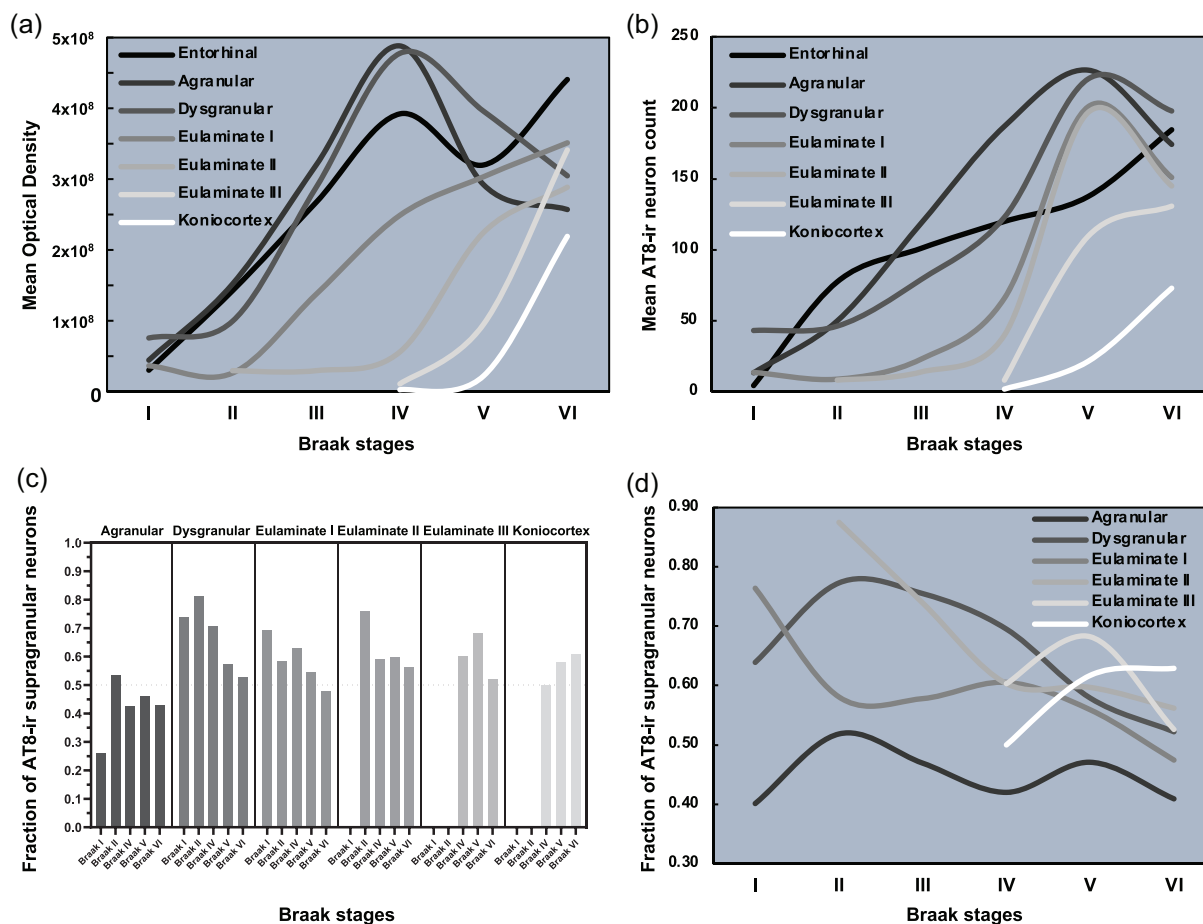


**FIGURE 11** Optical density (OD), AT8-ir neuron count, and fraction of AT8-ir supragranular neurons. (a) Mean AT8 immunostaining OD for layers I–VI across all the temporal cortical types in parallel to Braak stages; grayscale represents laminar complexity, from black (simplest cortical type) to white (most complex type). (b) Mean AT8-ir neuron counts for layers I–VI across all the temporal cortical types in parallel to Braak stages; grayscale represents laminar complexity, from black (simplest cortical type) to white (most complex type). (c, d) Fraction of AT8-ir supragranular neurons in all the Braak stages within each cortical type (c) and across all the temporal cortical types in parallel to Braak stages (d) [grayscale represents laminar complexity, from black (simplest cortical type) to lightest gray/white (most complex type)].

## 4 | DISCUSSION

We have used the antibody AT8 to quantify the spread of hyperphosphorylated tau across the temporal allo-, meso-, and isocortices in postmortem human brains with different Braak stages. In the pre-Braak stage, there were few AT8-ir neurons and neuropil treads in allocortical, mesocortical, eulaminate I, II, and III types. The number of AT8-ir neurons in these pre-Braak brains increased with age in the entorhinal cortex and the mesocortical and eulaminate types. In brains with Braak stages, AT8 immunostaining confirmed the dissemination of hyperphosphorylated tau from mesocortical transentorhinal areas toward isocortical areas described in the literature (Braak & Del Tredici, 2019). The laminar quantification of AT8-ir neurons showed that they were found preferentially in supragranular layers in the earliest Braak stages in each de novo involved neocortical type, but, as AD progressed, AT8-ir neurons tended to be equally distributed in supra- and infragranular layers. These laminar patterns of hyperphosphorylated tau spread (early in supragranular; late in supra- and infragranular layers) are compatible with the laminar patterns of cortico-cortical

synaptic connections predicted by the Structural Model (Barbas & Rempel-Clower, 1997; García-Cabezas et al., 2019). In the following sections, we comment the implications of these findings for studies of comparative neuroanatomy and of selective vulnerability of human mesocortical areas to AD.

### 4.1 | Hyperphosphorylated tau in nondemented subjects: Transentorhinal and more

We found scant AT8-ir neurons and neuropil treads in allocortical, mesocortical, and eulaminate types of the temporal lobe in nondemented young donors (Figures 4 and 5). This is not a surprising finding because neurofibrillary tangle pathology has been showed in large series of nondemented human brains obtained at autopsy (Braak & Braak, 1997). Actually, 50% of postmortem human brains at the age of 47 have neurofibrillary pathology equivalent to Braak stage I (Duyckaerts, 2011). In their autopsy series studies, the Braaks stated that the first cortical neurons involved in tangle pathology were in

the transentorhinal cortex (Braak & Braak, 1991, 1997). Surprisingly, in the three pre-Braak brains that we examined there were AT8-ir neurons in the mesocortical areas of the transentorhinal cortex, but also in proper (fascia dentata, cornu ammonis, and subiculum) and modified (presubiculum, parasubiculum, and entorhinal cortex) allocortical areas of the hippocampal formation and in eulaminar (isocortical) areas (Figures 4 and 5). This discrepancy with the classic studies of the Braaks could be due to differences in tissue sampling and processing. The Braaks sampled temporal lobe blocks at the mid uncus level (Braak & Braak, 1997), which roughly matches our amygdala level (e.g., Figures 4c and 5), while in the present article we analyzed four sections at four different levels: temporal pole, amygdala, anterior hippocampus, and posterior hippocampus. Also, the Braaks used classic silver impregnation techniques for labeling neurofibrillary tangles, but we used immunohistochemistry with the sensitive primary antibody AT8. Our findings suggest that the first accumulation of hyperphosphorylated tau is not restricted to mesocortical neurons in the transentorhinal cortex: it seems to start at mesocortical and eulaminar areas and then progresses into the allocortex (proper and modified) and along the neocortex toward the koniocortex. The exact place or places where hyperphosphorylated tau starts to accumulate in the cerebral cortex will be determined in further studies using larger series of postmortem human brains from young and nondemented donors. These studies will require adequate tissue sampling, including at least four coronal sections per temporal lobe, to confirm or correct our preliminary observations.

## 4.2 | Hyperphosphorylated tau seems to spread anterograde and retrogradely

An interesting finding in the present article is the two AT8 immunostaining patterns of neurons that we found in the pre-Braak and Braak staged brains. Some AT8-ir neurons had lightly labeled granules in their bodies, the most proximal dendritic segments, and initial axon segment and were surrounded by unstained neuropil (Figure 4f and g); these immunostaining patterns suggest that hyperphosphorylated tau reached the neuron body of the affected neurons by retrograde axon transportation. In contrast, other AT8-ir neuropil treads seemed to emanate from a single unlabeled neuron body like if they corresponded to distal dendritic segments (Figure 4h) and some AT8-ir neurons were densely labeled in their body and the proximal and distal dendritic segments (Figure 4i and j), like if they have been filled with hyperphosphorylated tau from the distal dendrites to the neuron body; this immunostaining pattern has been described by Braak and Del Tredici (2018) and suggests that hyperphosphorylated tau reached the distal dendrites of the affected neuron by transsynaptic spread after anterograde transportation along the axon of presynaptic neurons; then, from the distal dendrites, hyperphosphorylated tau progressed toward the neuron body and the axon until, probably, reaching another neuron postsynaptically. Therefore, it seems that that hyperphosphorylated tau spreads along the human cerebral cortex both anterograde and retrogradely.

## 4.3 | The principles of the Structural Model apply to the human neocortex

The credible demonstration of synaptic connections between two parts of the brain (e.g., two cortical areas) requires the use of synaptic tract-tracing techniques in laboratory animals. These techniques consist in *in vivo* injecting neural tracers that are up taken by neurons or synaptic terminals in the injection site. Then, the neural tracer is transported anterogradely (from the neurons that up took the tracer in the injection site to their axon terminals in distant projection targets) or retrogradely (from the synaptic terminals that up took the tracer in the injection site to their neuron bodies in distant projection origins). After a period to let the tracers be transported, the animal must be sacrificed and its brain processed to reveal the tracer in the structures where it was transported (Aparicio-Rodríguez & García-Cabezas, 2023; Lanciego & Wouterlood, 2020). These techniques can trace pathways to their origin or termination in cortical layers (e.g., Rockland & Pandya, 1979), even to the level of the synapse using electron microscopy (e.g., García-Cabezas & Barbas, 2017).

For obvious reasons, tract-tracing techniques are not applicable to the human brain; thus, contemporary researchers have turned to “trace” human brain pathways using *in vivo* image techniques. Such studies in the human cerebral cortex have showed that patterns of laminar thickness (estimated by MRI) and structural connections (as seen by tractography) are related (e.g., Saberi et al., 2023), but image techniques do not have enough resolution to trace pathways to the level of synapses (Grisot et al., 2021), nor to their origin or termination layers. Therefore, synaptic tract-tracing studies in nonhuman primates provide indispensable information for inferring synaptic pathways in the human brain. In this sense, the principles of the Structural Model, which were discovered in tract-tracing experiments in macaques (Barbas, 1986; Barbas & Rempel-Clower, 1997), could be *a priori* applicable to the human cerebral cortex. Accordingly, if the cortical type of two given parts of the human cerebral cortex is known, then we could infer the laminar pattern of connections between these parts. In the present article, by quantifying hyperphosphorylated tau across layers and types of the temporal cortex in postmortem human brains with different AD stages, we contribute a proof of concept of the validity of the Structural Model for predicting the laminar patterns of cortico-cortical connections in the human brain. We have found that, as AD progresses, the number of AT8-ir neurons does not increase equally in supra- and infragranular layers of the cortical types in the temporal lobe (Figure 11c and d). On the contrary, from the dysgranular toward the koniocortical type the fraction of AT8-ir supragranular neurons is higher in the early Braak stages and decreases and approaches the 0.5 value [equal number of AT8-ir neurons in supra- (II–III) and infragranular (V–VI) layers] in late Braak stages; in the eulaminar III and the koniocortical types, the last to be affected by AD progression, there are more AT8-ir neurons in the supra- (II–III) than in the infragranular (V–VI) layers. In contrast, in the agranular type the fraction of AT8-ir supragranular neurons increases and approaches the 0.5 value as AD progresses (Figure 11c and d). All these findings suggest that hyperphosphorylated tau disseminates from the dysgranular type, where

AT8 immunostaining is dense in early Braak stages (Figure 6j), toward the supragranular (II–III) layers of more complex cortical types and to the infragranular (V–VI) layers of the simpler agranular type. These laminar patterns of hyperphosphorylated tau dissemination are consistent with the principles of the Structural Model (Figure 2a). Accordingly, hyperphosphorylated tau probably spreads from the supragranular layers of dysgranular areas to the infragranular layers of agranular areas; such spread could follow both feedback and feedforward pathways. Also, the population of AT8-ir neurons in the infragranular layers of dysgranular areas, which are as many 1/3 of AT8-ir neurons in the supragranular layers (see Figure 10e and f), is probably enough to seed hyperphosphorylated tau in the supragranular layers of eulaminate I areas through feedback pathways. Alternatively, supragranular neurons in eulaminate I areas could retrogradely transport hyperphosphorylated tau from the infragranular layers in the dysgranular areas. The principles of the Structural Model can be used to identify potential pathways for prion-like progression of other neurodegenerative diseases, but also for the dissemination of epileptic seizures.

The lower levels of AT8 immunostaining in layer IV compared to the other cortical layers can also be explained by the laminar patterns of cortico-cortical connections traced in nonhuman primates. Layer IV is composed mostly of small interneurons that do not issue projections outside their cortical area (Barbas, 2015; García-Cabezas & Barbas, 2014a). This suggests that, as AD progresses from one isocortical type to another, hyperphosphorylated tau first arrives to supragranular (II–III) projection neurons, then to infragranular projection neurons (V–VI), and, finally, to the interneurons in layer IV by local connections.

Finally, the spread of hyperphosphorylated tau from meso- and isocortical areas to the superficial layers of the entorhinal cortex could also be explained by the patterns of synaptic connections between this modified allocortical area and the neocortical areas. The entorhinal cortex issues projections from deep and superficial layers that target the supragranular layers of temporal mesocortical areas (see figures 7 and 9 in Muñoz & Insausti, 2005, for origin of entorhinal projections to temporal mesocortices; see figure 8 in Suzuki & Amaral, 1994, for termination of entorhinal projections in temporal mesocortices). In the reverse direction, mesocortical areas issue projections to the entorhinal cortex that are originated mostly from the supragranular layers (see figure 17 in Insausti et al., 1987) and terminate in all entorhinal layers but preferentially in the superficial layers (Insausti & Amaral, 2008). Thus, hyperphosphorylated tau could reach the superficial layers of the entorhinal cortex from the supragranular layers of mesocortical temporal areas either by retrograde or anterograde transport. It is important to note that the principles of the Structural Model were discovered tracing cortico-cortical connections between neocortical areas, whose layers can be sorted into supra- and infragranular layers. The Structural Model does not make explicit predictions about laminar connections between allo- and neocortical areas because superficial and deep allocortical layers are not equivalent to the supra- and infragranular neocortical layers. This lack of equivalence is reflected in the different laminar pattern of subcortical projections of entorhinal and neocortical areas. Projections to the thalamus from neocortical areas are originated in infragranular (V–VI) layers (e.g., McFarland & Haber,

2002; Xiao et al., 2009); in contrast, entorhinal projections to the thalamus are originated in superficial and deep layers (see figure 6 in Saunders et al., 2005). Neocortical projection neurons to the striatum are restricted to layer V (Jones et al., 1977); in contrast, entorhinal projection neurons to the nucleus accumbens are more abundant in deep layers Va and b, but they are also present in superficial layers II and III (see figures 2 and 3 in Ohara et al., 2021). Thus, the six entorhinal layers issue projections to subcortical structures, while in the neocortex these projections are issued exclusively by infragranular (V–VI) layers. Based on these patterns of subcortical connections, we could consider that the six entorhinal layers and the infragranular (V–VI) neocortical layers are a kind of analogues; then, pathways from the entorhinal cortex to temporal mesocortical areas could be considered feedback and, in the reverse direction, from temporal mesocortical areas to the entorhinal cortex could be considered feedforward, as the Structural Model would have predicted. The idea of considering all the layers of allocortical areas as analogues of infragranular layers of neocortical areas is highly speculative, but it could explain the laminar pattern of connections between entorhinal and temporal neocortical areas, as well as hyperphosphorylated tau spreading, within the frame of the Structural Model.

#### 4.4 | Mesocortical areas: Phylogenetic and connective vulnerability

A key question in AD research is why temporal mesocortical areas are more vulnerable to neurodegeneration. This question can be addressed from a phylogenetic point of view in the frame of the Hypothesis on the Dual Origin of the Neocortex, according to which the mesocortical ring is older than the isocortical island. One could ask whether mesocortical areas are also vulnerable to neurodegeneration in other mammals, but the typical neuritic plaques and A $\beta$  amyloid deposits in small blood vessel walls of AD and a mild taupathy have been described only in nonhuman primates. Importantly, the distribution pattern and extent of hyperphosphorylated tau inclusions in nonhuman primates never approximate the abundance of neurofibrillary tangles and neuropil threads in human subjects with AD (reviewed in Arendt et al., 2017; Heuer et al., 2012; Hof et al., 2002; Walker & Jucker, 2017). These findings suggest that, from a phylogenetic point of view, an incomplete form of AD-like pathology, including A $\beta$  amyloid neuritic plaques and hyperphosphorylated tau neurofibrillary tangles, emerged in nonhuman primates but fully developed only in human AD. Some researchers have suggested that the genetic changes underlying the quantitative and qualitative expansion of the human brain may have increased the susceptibility of human neurons to factors that lead to AD; for instance, some cortical areas do not completely mature and retain increased synaptic plasticity and metabolic activity in adult life, what may render them more vulnerable to AD (Barbas, 1995; Buřill et al., 2013). This seems to be the case of mesocortical areas that have higher expression of epigenetic regulators (Sancha-Velasco et al., 2023) and markers that favor synaptic plasticity (García-Cabezas et al., 2017) than eulaminate areas and show hyperphosphorylated tau inclusions in the early AD stages (Figure 6j).

Mesocortical areas also have an extra factor of vulnerability related to their cortico-cortical connections. We have showed that, while agranular and koniocortical types at the extremes of the gradient of laminar complexity have most of their connections with adjacent types, the dysgranular and eulaminate I, II, and III types have more widespread cortical connections (see figure 4b in Aparicio-Rodríguez & García-Cabezas, 2023; see also summary figures in Morecraft et al., 2004; Morecraft et al., 2012; Morecraft et al., 2015). Such connective spread of mesocortical neurons may require higher metabolic costs, which can be an extra burden for the less stable and more plastic dysgranular projection neurons.

#### 4.5 | Limitations of this study

In the present article, we analyzed AT8 immunostaining in four sections at four different anterior–posterior levels of the temporal lobe from eight postmortem human brains. With such limited sampling and small brain sample we have offered a proof of concept for the validity of the Structural Model in the human cerebral cortex; also, we have found that hyperphosphorylated tau accumulates in young non-demented subjects at the transentorhinal cortex, as described by Braak and Braak (1991, 1997), but also at other allo-, meso-, and isocortical sites (Figures 4 and 5). Our findings will have to be confirmed by further studies with more brains. Also, we have limited the analysis of hyperphosphorylated tau spreading to the temporal lobe, but other cortical regions, like the insula and cingulate areas, are affected by AD (Braak et al., 2006); further studies could extend the laminar quantification of AT8-ir neurons to these and other cortical areas. Finally, the distribution of AT8-ir neurons could be studied in postmortem brains from donors with other tauopathies, like chronic traumatic encephalopathy, to confirm the validity of the Structural Model principles in the human cerebral cortex.

## 5 | CONCLUSIONS

In the present article, we show that hyperphosphorylated tau initially accumulates in allo-, meso-, and isocortical areas of the temporal lobe. Also, we show that hyperphosphorylated tau spreads along the human neocortex in laminar patterns that match the laminar patterns of cortico-cortical connections predicted by the Structural Model. Although further studies are needed to confirm our findings, we present a proof of concept of the validity of the Structural Model. This model could be applied to infer the organization of cortical circuits and synaptic pathways in the human cerebral cortex that could be relevant for neurodegeneration progression or epilepsy. Our study also highlights the relevance on nonhuman primate tract-tracing studies, which are becoming more uncommon every year, to provide fundamental data for understanding human neuropathology.

#### ACKNOWLEDGMENTS

We gratefully acknowledge the human brain donors and their relatives. We also thank Dr. Carmen Cavada and the personnel at the

Plataforma Biobanco - Instituto Murciano de Investigación Biosanitaria Pascual Parrilla and the Banco de Tejidos de la Fundación CIEN for their cooperation in obtaining the postmortem human brain tissue. MAG-C was the recipient of a Beatriz Galindo senior research position in the School of Medicine at Universidad Autónoma de Madrid (BEAGAL18/00098) and of a Grant for I+D Projects to the Beatriz Galindo Program Researchers at Universidad Autónoma de Madrid (SI2/PBG/2020-00014) from the Madrid Government (Comunidad de Madrid-Spain) under the Multiannual Agreement with Universidad Autónoma de Madrid in the line of action encouraging young research doctors, in the context of the V PRICIT (Regional Program of Research and Technological Innovation).

#### CONFLICT OF INTEREST STATEMENT

The authors declare that they have no competing interests, or other interests that might be perceived to influence the results and/or discussion reported in this article.

#### DATA AVAILABILITY STATEMENT

The data that support the findings of this study are available in the supporting file [cne25623-sup-0001-SuppMat.xlsx](#).

#### ORCID

Alicia Uceda-Heras  <https://orcid.org/0000-0001-6157-7098>

Gonzalo Aparicio-Rodríguez  <https://orcid.org/0000-0002-9757-1541>

Miguel Ángel García-Cabezas  <https://orcid.org/0000-0003-0534-5182>

#### PEER REVIEW

The peer review history for this article is available at <https://publons.com/publon/10.1002/cne.25623>.

#### REFERENCES

- Alafuzoff, I., Arzberger, T., Al-Sarraj, S., Bodi, I., Bogdanovic, N., Braak, H., Bugiani, O., Del-Tredici, K., Ferrer, I., Gelpi, E., Giaccone, G., Graeber, M. B., Ince, P., Kamphorst, W., King, A., Korkolopoulou, P., Kovács, G. G., Larionov, S., Meyronet, D., ... Kretzschmar, H. (2008). Staging of neurofibrillary pathology in Alzheimer's disease: A study of the BrainNet Europe Consortium. *Brain Pathology*, 18(4), 484–496. <https://doi.org/10.1111/j.1750-3639.2008.00147.x>
- Aparicio-Rodríguez, G., & García-Cabezas, M. Á. (2023). Comparison of the predictive power of two models of cortico-cortical connections in primates: The distance rule model and the structural model. *Cerebral Cortex*, 33(13), 8131–8149. <https://doi.org/10.1093/cercor/bhad104>
- Arendt, T., Stieler, J., & Ueberham, U. (2017). Is sporadic Alzheimer's disease a developmental disorder? *Journal of Neurochemistry*, 143(4), 396–408. <https://doi.org/10.1111/jnc.14036>
- Arnold, S. E., Hyman, B. T., Flory, J., Damasio, A. R., & Van Hoesen, G. W. (1991). The topographical and neuroanatomical distribution of neurofibrillary tangles and neuritic plaques in the cerebral cortex of patients with Alzheimer's disease. *Cerebral Cortex*, 1(1), 103–116. <https://doi.org/10.1093/cercor/1.1.103>
- Barbas, H. (1986). Pattern in the laminar origin of corticocortical connections. *Journal of Comparative Neurology*, 252(3), 415–422. <https://doi.org/10.1002/cne.902520310>
- Barbas, H. (1995). Anatomic basis of cognitive-emotional interactions in the primate prefrontal cortex. *Neuroscience and Biobehavioral Reviews*, 19, 499–510. [https://doi.org/10.1016/0149-7634\(94\)00053-4](https://doi.org/10.1016/0149-7634(94)00053-4)



- Barbas, H. (1997). Cortical structure predicts the pattern of corticocortical connections. *Cerebral Cortex*, 7(7), 635–646. <https://doi.org/10.1093/cercor/7.7.635>
- Barbas, H. (2015). General cortical and special prefrontal connections: Principles from structure to function. *Annual Review of Neuroscience*, 38, 269–289. <https://doi.org/10.1146/annurev-neuro-071714-033936>
- Barbas, H., & García-Cabezas, M. Á. (2016). How the prefrontal executive got its stripes. *Current Opinion in Neurobiology*, 40, 125–134. <https://doi.org/10.1016/j.conb.2016.07.003>
- Barbas, H., & Hilgetag, C. C. (2023). From circuit principles to human psychiatric disorders. *Biological Psychiatry*, 93(5), 388–390. <https://doi.org/10.1016/j.biopsych.2022.08.007>
- Barbas, H., Wang, J., Joyce, M. K. P., & García-Cabezas, M. Á. (2018). Pathway mechanism for excitatory and inhibitory control in working memory. *Journal of Neurophysiology*, 120(5), 2659–2678. <https://doi.org/10.1152/jn.00936.2017>
- Bautista, J., García-Cabezas, M. Á., Medalla, M., Rosene, D. L., Zikopoulos, B., & Barbas, H. (2023). Pattern of ventral temporal lobe interconnections in rhesus macaques. *Journal of Comparative Neurology*, 531, 1963–1986. <https://doi.org/10.1002/cne.25550>
- Beul, S. F., Barbas, H., & Hilgetag, C. C. (2017). A predictive structural model of the primate connectome. *Scientific Reports*, 7, 43176. <https://doi.org/10.1038/srep43176>
- Braak, H., Alafuzoff, I., Arzberger, T., Kretschmar, H., & Del Tredici, K. (2006). Staging of Alzheimer disease-associated neurofibrillary pathology using paraffin sections and immunocytochemistry. *Acta Neuropathologica*, 112(4), 389–404. <https://doi.org/10.1007/s00401-006-0127-z>
- Braak, H., & Braak, E. (1991). Neuropathological staging of Alzheimer-related changes. *Acta Neuropathologica*, 82(4), 239–259. <https://doi.org/10.1007/BF00308809>
- Braak, H., & Braak, E. (1997). Frequency of stages of Alzheimer-related lesions in different age categories. *Neurobiology of Aging*, 18(4), 351–357. [https://doi.org/10.1016/s0197-4580\(97\)00056-0](https://doi.org/10.1016/s0197-4580(97)00056-0)
- Braak, H., & Del Tredici, K. (2011). Alzheimer's pathogenesis: Is there neuron-to-neuron propagation? *Acta Neuropathologica*, 121(5), 589–595. <https://doi.org/10.1007/s00401-011-0825-z>
- Braak, H., & Del Tredici, K. (2018). Spreading of tau pathology in sporadic Alzheimer's disease along cortico-cortical top-down connections. *Cerebral Cortex*, 28(9), 3372–3384. <https://doi.org/10.1093/cercor/bhy152>
- Braak, H., & Del Tredici, K. (2019). Top-down projections direct the gradual progression of Alzheimer-related tau pathology throughout the neocortex. *Advances in Experimental Medicine and Biology*, 1184, 291–303. [https://doi.org/10.1007/978-981-32-9358-8\\_22](https://doi.org/10.1007/978-981-32-9358-8_22)
- Buflin, E., Blesa, R., & Augusti, J. (2013). Alzheimer's disease: An evolutionary approach. *Journal of Anthropological Sciences*, 91, 135–157. <https://doi.org/10.4436/jass.91001>
- Calderon-Garcidueñas, A. L., & Duyckaerts, C. (2017). Alzheimer disease. *Handbook of Clinical Neurology*, 145, 325–337. <https://doi.org/10.1016/B978-0-12-802395-2.00023-7>
- Chanes, L., & Barrett, L. F. (2016). Redefining the role of limbic areas in cortical processing. *Trends in Cognitive Sciences*, 20(2), 96–106. <https://doi.org/10.1016/j.tics.2015.11.005>
- Duyckaerts, C. (2011). Tau pathology in children and young adults: Can you still be unconditionally baptist? *Acta Neuropathologica*, 121(2), 145–147. <https://doi.org/10.1007/s00401-010-0794-7>
- Felleman, D. J., & Van Essen, D. C. (1991). Distributed hierarchical processing in the primate cerebral cortex. *Cerebral Cortex*, 1, 1–47. <https://doi.org/10.1093/cercor/1.1.1>
- García-Cabezas, M. Á., & Barbas, H. (2014a). Area 4 has layer IV in adult primates. *European Journal of Neuroscience*, 39(11), 1824–1834. <https://doi.org/10.1111/ejn.12585>
- García-Cabezas, M. Á., & Barbas, H. (2014b). A direct anterior cingulate pathway to the primate primary olfactory cortex may control attention to olfaction. *Brain Structure & Function*, 219(5), 1735–1754. <https://doi.org/10.1007/s00429-013-0598-3>
- García-Cabezas, M. Á., & Barbas, H. (2017). Anterior cingulate pathways may affect emotions through orbitofrontal cortex. *Cerebral Cortex*, 27(10), 4891–4910. <https://doi.org/10.1093/cercor/bhw284>
- García-Cabezas, M. Á., Hacker, J. L., & Zikopoulos, B. (2020). A protocol for cortical type analysis of the human neocortex applied on histological samples, the Atlas of Von Economo and Koskinas, and magnetic resonance imaging. *Frontiers in Neuroanatomy*, 14, 576015. <https://doi.org/10.3389/fnana.2020.576015>
- García-Cabezas, M. Á., Hacker, J. L., & Zikopoulos, B. (2023a). Homology of neocortical areas in rats and primates based on cortical type analysis: An update of the Hypothesis on the Dual Origin of the Neocortex. *Brain Structure & Function*, 228(5), 1069–1093. <https://doi.org/10.1007/s00429-022-02548-0>
- García-Cabezas, M. Á., Joyce, M. K. P., John, Y. J., Zikopoulos, B., & Barbas, H. (2017). Mirror trends of plasticity and stability indicators in primate prefrontal cortex. *European Journal of Neuroscience*, 46(8), 2392–2405. <https://doi.org/10.1111/ejn.13706>
- García-Cabezas, M. Á., Pérez-Santos, I., & Cavada, C. (2023b). Stereotaxic cutting of post-mortem human brains for neuroanatomical studies. *Frontiers in Neuroanatomy*, 17, 1176351. <https://doi.org/10.3389/fnana.2023.1176351>
- García-Cabezas, M. Á., Rico, B., Sánchez-González, M. Á., & Cavada, C. (2007). Distribution of the dopamine innervation in the macaque and human thalamus. *Neuroimage*, 34(3), 965–984. <https://doi.org/10.1016/j.neuroimage.2006.07.032>
- García-Cabezas, M. Á., & Zikopoulos, B. (2019). Evolution, development, and organization of the cortical connectome. *PLoS Biology*, 17(5), e3000259. <https://doi.org/10.1371/journal.pbio.3000259>
- García-Cabezas, M. Á., Zikopoulos, B., & Barbas, H. (2019). The Structural Model: A theory linking connections, plasticity, pathology, development and evolution of the cerebral cortex. *Brain Structure & Function*, 224(3), 985–1008. <https://doi.org/10.1007/s00429-019-01841-9>
- Goedert, M., Jakes, R., & Vanmechelen, E. (1995). Monoclonal antibody AT8 recognises tau protein phosphorylated at both serine 202 and threonine 205. *Neuroscience Letters*, 189(3), 167–170. [https://doi.org/10.1016/0304-3940\(95\)11484-E](https://doi.org/10.1016/0304-3940(95)11484-E)
- Gonzalez-Arnav, E., Perez-Santos, I., Jimenez-Sanchez, L., Cid, E., Gal, B., de la Prida, L. M., & Cavada, C. (2024). Immunohistochemical field parcelation of the human hippocampus along its antero-posterior axis. *Brain Structure & Function*, 229(2), 359–385. <https://doi.org/10.1007/s00429-023-02725-9>
- Grisot, G., Haber, S. N., & Yendiki, A. (2021). Diffusion MRI and anatomic tracing in the same brain reveal common failure modes of tractography. *Neuroimage*, 239, 118300. <https://doi.org/10.1016/j.neuroimage.2021.118300>
- Heuer, E., F. Rosen, R., Cintron, A., & C Walker, L. (2012). Nonhuman primate models of Alzheimer-like cerebral proteopathy. *Current Pharmaceutical Design*, 18(8), 1159–1169. <https://doi.org/10.2174/138161212799315885>
- Hilgetag, C. C., Beul, S. F., Van Albada, S. J., & Goulas, A. (2019). An architectonic type principle integrates macroscopic cortico-cortical connections with intrinsic cortical circuits of the primate brain. *Network Neuroscience*, 3(4), 905–923. [https://doi.org/10.1162/netn\\_a\\_00100](https://doi.org/10.1162/netn_a_00100)
- Hilgetag, C. C., & Goulas, A. (2020). 'Hierarchy' in the organization of brain networks. *Philosophical Transactions of the Royal Society of London. Series B: Biological Sciences*, 375(1796), 20190319. <https://doi.org/10.1098/rstb.2019.0319>
- Hilgetag, C. C., Medalla, M., Beul, S. F., & Barbas, H. (2016). The primate connectome in context: Principles of connections of the cortical visual system. *Neuroimage*, 134, 685–702. <https://doi.org/10.1016/j.neuroimage.2016.04.017>
- Hof, P. R., Gilisen, E. P., Sherwood, C. C., Duan, H., Lee, P. W. H., Delman, B. N., Naidich, T. P., Gannon, P. J., Perl, D. P., & Erwin, J. M. (2002). Comparative neuropathology of brain aging in primates. In J. M. Erwin, & P. R. Hof (Eds.), *Aging in nonhuman primates* (Vol. 31, pp. 239). Karger, Basel.

- Insausti, R., & Amaral, D. G. (2008). Entorhinal cortex of the monkey: IV. Topographical and laminar organization of cortical afferents. *Journal of Comparative Neurology*, 509(6), 608–641. <https://doi.org/10.1002/cne.21753>
- Insausti, R., Amaral, D. G., & Cowan, W. M. (1987). The entorhinal cortex of the monkey: II. Cortical afferents. *Journal of Comparative Neurology*, 264(3), 356–395. <https://doi.org/10.1002/cne.902640306>
- Insausti, R., Cebada-Sanchez, S., & Marcos, P. (2010). Postnatal development of the human hippocampal formation. *Advances in Anatomy, Embryology and Cell Biology*, 206, 1–86. [https://doi.org/10.1007/978-3-642-03661-3\\_1](https://doi.org/10.1007/978-3-642-03661-3_1)
- Jones, E. G., Coulter, J. D., Burton, H., & Porter, R. (1977). Cells of origin and terminal distribution of corticostriatal fibers arising in the sensory-motor cortex of monkeys. *Journal of Comparative Neurology*, 173(1), 53–80. <https://doi.org/10.1002/cne.901730105>
- Joyce, M. K. P., & Barbas, H. (2018). Cortical connections position primate area 25 as a keystone for interoception, emotion, and memory. *Journal of Neuroscience*, 38(7), 1677–1698. <https://doi.org/10.1523/JNEUROSCI.2363-17.2017>
- Lanciego, J. L., & Wouterlood, F. G. (2020). Neuroanatomical tract-tracing techniques that did go viral. *Brain structure & Function*, 225(4), 1193–1224. <https://doi.org/10.1007/s00429-020-02041-6>
- Mcfarland, N. R., & Haber, S. N. (2002). Thalamic relay nuclei of the basal ganglia form both reciprocal and nonreciprocal cortical connections, linking multiple frontal cortical areas. *Journal of Neuroscience*, 22, 8117–8132. <https://doi.org/10.1523/JNEUROSCI.22-18-08117.2002>
- Medalla, M., & Barbas, H. (2006). Diversity of laminar connections linking periarculate and lateral intraparietal areas depends on cortical structure. *European Journal of Neuroscience*, 23(1), 161–179. <https://doi.org/10.1111/j.1460-9568.2005.04522.x>
- Medalla, M., & Barbas, H. (2014). Specialized prefrontal “auditory fields”: Organization of primate prefrontal-temporal pathways. *Frontiers in Neuroscience*, 8, 77. <https://doi.org/10.3389/fnins.2014.00077>
- Morecraft, R. J., Cipolloni, P. B., Stilwell-Morecraft, K. S., Gedney, M. T., & Pandya, D. N. (2004). Cytoarchitecture and cortical connections of the posterior cingulate and adjacent somatosensory fields in the rhesus monkey. *Journal of Comparative Neurology*, 469(1), 37–69. <https://doi.org/10.1002/cne.10980>
- Morecraft, R. J., Stilwell-Morecraft, K. S., Cipolloni, P. B., Ge, J., Mcneal, D. W., & Pandya, D. N. (2012). Cytoarchitecture and cortical connections of the anterior cingulate and adjacent somatomotor fields in the rhesus monkey. *Brain Research Bulletin*, 87(4–5), 457–497. <https://doi.org/10.1016/j.brainresbull.2011.12.005>
- Morecraft, R. J., Stilwell-Morecraft, K. S., Ge, J., Cipolloni, P. B., & Pandya, D. N. (2015). Cytoarchitecture and cortical connections of the anterior insula and adjacent frontal motor fields in the rhesus monkey. *Brain Research Bulletin*, 119(Pt A), 52–72. <https://doi.org/10.1016/j.brainresbull.2015.10.004>
- Muñoz, M., & Insausti, R. (2005). Cortical efferents of the entorhinal cortex and the adjacent parahippocampal region in the monkey (*Macaca fascicularis*). *European Journal of Neuroscience*, 22(6), 1368–1388. <https://doi.org/10.1111/j.1460-9568.2005.04299.x>
- Nieuwenhuys, R., Voogd, J., & Cv, H. (2008). *The human central nervous system* (4th ed.). Springer.
- Ohara, S., Yoshino, R., Kimura, K., Kawamura, T., Tanabe, S., Zheng, A., Nakamura, S., Inoue, K.-I., Takada, M., Tsutsui, K.-I., & Witter, M. P. (2021). Laminar organization of the entorhinal cortex in Macaque Monkeys based on cell-type-specific markers and connectivity. *Frontiers in Neural Circuits*, 15, 790116. <https://doi.org/10.3389/fncir.2021.790116>
- Puelles, L., Alonso, A., García-Calero, E., & Martínez-De-La-Torre, M. (2019). Concentric ring topology of mammalian cortical sectors and relevance for patterning studies. *Journal of Comparative Neurology*, 527(10), 1731–1752. <https://doi.org/10.1002/cne.24650>
- Rempel-Clower, N. L., & Barbas H (2000). The laminar pattern of connections between prefrontal and anterior temporal cortices in the Rhesus monkey is related to cortical structure and function. *Cerebral Cortex*, 10(9), 851–865. <https://doi.org/10.1093/cercor/10.9.851>
- Rockland, K. S., & Pandya, D. N. (1979). Laminar origins and terminations of cortical connections of the occipital lobe in the rhesus monkey. *Brain Research*, 179, 3–20. [https://doi.org/10.1016/0006-8993\(79\)90485-2](https://doi.org/10.1016/0006-8993(79)90485-2)
- Ruiz-Cabrera, S., Pérez-Santos, I., Zaldivar-Diez, J., & García-Cabezas, M. Á. (2023). Expansion modes of primate nervous system structures in the light of the Prosomeric Model. *Frontiers in Mammal Science*, 2, 1241573. <https://doi.org/10.3389/fmamm.2023.1241573>
- Saberi, A., Paquola, C., Wagstyl, K., Hettwer, M. D., Bernhardt, B. C., Eickhoff, S. B., & Valk, S. L. (2023). The regional variation of laminar thickness in the human isocortex is related to cortical hierarchy and interregional connectivity. *PLoS Biology*, 21(11), e3002365. <https://doi.org/10.1371/journal.pbio.3002365>
- Sancha-Velasco, A., Uceda-Heras, A., & García-Cabezas, M. Á. (2023). Cortical type: A conceptual tool for meaningful biological interpretation of high-throughput gene expression data in the human cerebral cortex. *Frontiers in Neuroanatomy*, 17, 1187280. <https://doi.org/10.3389/fnana.2023.1187280>
- Sanides, F. (1962). Architectonics of the human frontal lobe of the brain. With a demonstration of the principles of its formation as a reflection of phylogenetic differentiation of the cerebral cortex. *Monographien Aus Dem Gesamtgebiete Der Neurologie Und Psychiatrie*, 98, 1–201.
- Sanides, F. (1970). Functional architecture of motor and sensory cortices in primates in the light of a new concept of neocortex evolution. In C. R. Noback, & W. Montagna (Eds.) *The primate brain: Advances in primatology*. (pp. 137–208). Appleton-Century-Crofts Educational Division/Meredith Corporation.
- Saunders, R. C., Mishkin, M., & Aggleton, J. P. (2005). Projections from the entorhinal cortex, perirhinal cortex, presubiculum, and parasubiculum to the medial thalamus in macaque monkeys: Identifying different pathways using disconnection techniques. *Experimental Brain Research*, 167(1), 1–16. <https://doi.org/10.1007/s00221-005-2361-3>
- Suzuki, W. A., & Amaral, D. G. (1994). Topographic organization of the reciprocal connections between the monkey entorhinal cortex and the perirhinal and parahippocampal cortices. *Journal of Neuroscience*, 14(3 Pt 2), 1856–1877. <https://doi.org/10.1523/JNEUROSCI.14-03-01856.1994>
- Walker, L. C., & Jucker, M. (2017). The exceptional vulnerability of humans to Alzheimer's disease. *Trends in Molecular Medicine*, 23(6), 534–545. <https://doi.org/10.1016/j.molmed.2017.04.001>
- Xiao, D., Zikopoulos, B., & Barbas, H. (2009). Laminar and modular organization of prefrontal projections to multiple thalamic nuclei. *Neuroscience*, 161(4), 1067–1081. <https://doi.org/10.1016/j.neuroscience.2009.04.034>

## SUPPORTING INFORMATION

Additional supporting information can be found online in the Supporting Information section at the end of this article.

**How to cite this article:** Uceda-Heras, A., Aparicio-Rodríguez, G., & García-Cabezas, M. Á. (2024). Hyperphosphorylated tau in Alzheimer's disease disseminates along pathways predicted by the Structural Model for Cortico-cortical Connections. *Journal of Comparative Neurology*, 532, e25623. <https://doi.org/10.1002/cne.25623>